JOURNAL OF GEOPHYSICAL RESEARCH, VOL. 114, C10001, doi:10.1029/2008JC004918, 2009

Click Here for Full Article

Investigation of the physical scaling of sea spray spume droplet production

C. W. Fairall,[1] M. L. Banner,[2] W. L. Peirson,[2,3] W. Asher,[4] and R. P. Morison[2]

Received 16 May 2008; revised 29 April 2009; accepted 17 June 2009; published 2 October 2009.

[1] In this paper we report on a laboratory study, the Spray Production and Dynamics Experiment (SPANDEX), conducted at the University of New South Wales Water Research Laboratory in Australia. The goals of SPANDEX were to illuminate physical aspects of spume droplet production and dispersion; verify theoretical simplifications used to estimate the source function from ambient droplet concentration measurements; and examine the relationship between the implied source strength and forcing parameters such as wind speed, surface turbulent stress, and wave properties. Observations of droplet profiles give reasonable confirmation of the basic power law profile relationship that is commonly used to relate droplet concentrations to the surface source strength. This essentially confirms that, even in a wind tunnel, there is a near balance between droplet production and removal by gravitational settling. The observations also indicate considerable droplet mass may be present for sizes larger than 1.5 mm diameter. Phase Doppler Anemometry observations revealed significant mean horizontal and vertical slip velocities that were larger closer to the surface. The magnitude seems too large to be an acceleration time scale effect. Scaling of the droplet production surface source strength proved to be difficult. The wind speed forcing varied only 23% and the stress increased a factor of 2.2. Yet, the source strength increased by about a factor of 7. We related this to an estimate of surface wave energy flux through calculations of the standard deviation of small-scale water surface disturbance, a wave-stress parameterization, and numerical wave model simulations. This energy index only increased by a factor of 2.3 with the wind forcing. Nonetheless, a graph of spray mass surface flux versus surface disturbance energy is quasi-linear with a substantial threshold.

Citation: Fairall, C. W., M. L. Banner, W. L. Peirson, W. Asher, and R. P. Morison (2009), Investigation of the physical scaling of sea spray spume droplet production, *J. Geophys. Res.*, *114*, C10001, doi:10.1029/2008JC004918.

1. Introduction

[2] Present parameterizations of air-sea turbulent fluxes are reasonably valid up to wind speeds of about 25 ms^{-1} [*Fairall et al.*, 2003; *Drennan et al.*, 2007]. This wind speed range covers the vast majority of oceanic wind climatology. However, forecasts of hurricane intensity are very sensitive to specification of the transfer coefficients at wind speeds up to 70 ms^{-1} [e.g., *Bao et al.*, 2000; *Wang et al.*, 2001; *Li*, 2004]. Extrapolations of the current parameterizations to hurricane wind speeds are inconsistent with theoretical analyses of the potential strength of tropical cyclones [*Emanuel*, 1995, 1999]. One major issue is the relative balance of momentum and scalar (heat/moisture) transfers, usually expressed as the ratio of the momentum to enthalpy transfer coefficient. There is recent evidence that the momentum transfer coefficient levels off at a wind speed of 30–40 ms^{-1} [*Powell et al.*, 2003; *French et al.*, 2007]. It is also speculated that the heat and moisture balance is affected by evaporation of sea spray droplets at very high wind speeds ($U > 25$ ms^{-1}). At high wind speeds, the ocean is a major source of droplets produced by bursting bubbles and spume (i.e., from sheared-off wave tops) to the lower troposphere [*Andreas et al.*, 1995]. Because of their much larger sizes (and larger mass flux) spume droplets are expected to dominate the hurricane droplet flux problem. Droplets may play a large role in latent heat transfer between the ocean and atmosphere [*Edson and Fairall.*, 1994; *Andreas et al.*, 1995; *Makin*, 1998] and under extremely high winds such as found in hurricanes, may also have a large effect on the air-sea exchange of momentum [*Andreas and Emanuel*, 2001; *Andreas*, 2004; *Barenblatt et al.*, 2005; *Makin*, 2005]. From a modeling perspective, there are two fundamental problems, (1) spec-

[1]Earth System Research Laboratory, NOAA, Boulder, Colorado, USA.
[2]School of Mathematics and Statistics, University of New South Wales, Sydney, New South Wales, Australia.
[3]Also at Water Research Laboratory, School of Civil and Environmental Engineering, University of New South Wales, Sydney, New South Wales, Australia.
[4]Applied Physics Laboratory, University of Washington, Seattle, Washington, USA.

Copyright 2009 by the American Geophysical Union.
0148-0227/09/2008JC004918$09.00

ification of the sea surface droplet source strength and (2) computation (or parameterization) of the thermodynamic effects of the sea spray [*Andreas*, 1992; *Fairall et al.*, 1994; *Kepert et al.*, 1999].

[3] The fundamental parameter required for representing the effect of sea spray on air-sea exchange processes is the size-dependent source function, $S_n(r)$, or number of droplets of a given size produced at the sea surface per unit surface area per unit time, as a function of the surface forcing (wind speed, wave breaking, surface stress, etc). Because the source function cannot be measured directly at present, it is typically estimated from the height-dependent number size distribution of droplets, $n(r, z)$ (see section 2). Current specifications of the source strength are based on laboratory studies, scaling arguments and a few field measurements at wind speeds less than 30 ms^{-1} [*Fairall et al.*, 1990; *Andreas*, 1998; *Kepert et al.*, 1999; *Andreas and Emanuel*, 2001]. Verification of droplet source parameterizations at high winds has been frustrated because of the difficulty of measuring $n(r, z)$ and/or near-surface turbulent fluxes in hurricanes. Thus, their application in hurricane models still amounts to extrapolation into a domain of great uncertainty.

[4] Current parameterizations of S_n are based on either wind speed or whitecap fraction which is usually represented as a function of wind speed [*Andreas and Emanuel*, 2001]. In recent years, parameterizations in terms of the physical processes that drive spume sea spray production have been sought. This is needed to aid in the interpretation of field measurements, extend the range of extrapolation, and account for the great spatial diversity in wind and wave balances in the hurricane environment. In contrast to the situation in bubble-mediated droplet fluxes, spume droplet production physics is much less explored. As a result, *Lewis and Schwartz* [2004] provide an assessment of the knowledge of large particle production that states "virtually nothing is known about this flux or its dependencies on particle size and wind speed."

[5] In 2002, the CBLAST program instituted a multipronged study of air-sea interaction at hurricane force wind speeds [*Black et al.*, 2007]. One component of the project includes theoretical development, laboratory studies, and airborne droplet measurements in tropical cyclones with both droplet surface source strength and thermodynamic interactions under investigation. In this paper we report on a laboratory study, the Spray Production and Dynamics Experiment (SPANDEX), done in January and February of 2003. SPANDEX was conducted at the University of New South Wales Water Research Laboratory in Manly Vale, Sydney, Australia. The goals of SPANDEX were to illuminate physical aspects of spume droplet production and dispersion, verify theoretical simplifications presently used to estimate the source function from ambient droplet concentration measurements, and examine the relationship between the implied source strength and forcing parameters such as wind speed, surface turbulent stress, and wave properties.

[6] In the remainder of this paper we will discuss basic droplet source and turbulent transport relationships (section 2), give some background on droplet source parameterizations and scaling arguments for the source function (section 3). Details on the SPANDEX instruments, set up, and forcing condition will be given in section 4. The results will be given in section 5; conclusions in section 6.

2. Droplet Dynamics and Concentration Profiles

2.1. Turbulent Transport Equations

[7] In reasonably horizontally homogenous conditions, the aerosol particle conservation equation [*Fairall et al.*, 1990] can be expressed

$$\frac{Dn}{Dt} = -\frac{\partial}{\partial z}\left[\overline{w'n'} - D_p\frac{\partial n}{\partial z} - V_g n + \overline{w_s'n'}\right] + Q_n \qquad (1)$$

where z is the height above surface, n the mean and n' fluctuations in the size-dependent droplet number concentration, w' the vertical air motion fluctuations, D_p the size-dependent droplet molecular diffusion coefficient, V_g the particle mean gravitational settling velocity, w_s' the air-particle slip velocity, and Q_n a particle size and height-dependent source function (number of particles of a specific size increment created per unit volume per second at a specified height). We move the volume source term inside the integral and write it as a flux

$$\frac{Dn}{Dt} = -\frac{\partial}{\partial z}\left[\overline{w'n'} - D_p\frac{\partial n}{\partial z} - V_g n + \overline{w_s'n'} + S_n\right] \qquad (2)$$

where

$$S_n = \int_z^\infty Q_n(z)dz \qquad (3)$$

We can then write a flux variable that includes the source terms

$$F_z = \left[\overline{w'n'} - D_p\frac{\partial n}{\partial z} - V_g n + \overline{w_s'n'} + S_n\right] \qquad (4)$$

When the concentration profile is near equilibrium, the term inside the derivative is independent of height. Near the ocean surface, this is a weak constraint providing z is much less than the depth of the boundary layer. In this surface layer, the total "flux" at z is essentially the same as at the top of the molecular diffusive sublayer. We do not actually require equilibrium, only that the quantity $z\,Dn/Dt$ is small compared to the individual terms in F_z. In the wind tunnel experiment (see section 4) the droplet observations are made in a well-developed boundary layer considerably downwind (about 30 boundary layer depths) from the initial breaking zone so that the droplet concentration is not changing significantly with fetch. Thus, we expect advection to be negligible in the balance expressed by (2).

[8] The production of sea spray droplets is confined very close to the surface in a source region below the height h. Thus, we can deal with the dynamics of interest here by assuming $F_z = F_o$ equals constant for heights less than a few times h. Bubble-generated droplets tend to be characterized by near-vertical ejection from the interface with an initial velocity so that in a fraction of a second they reach a height of several cm above the surface where they join the general background of turbulent fluid motions. Spume droplets are

blown off the top of breaking regions near the windward face of the dominant waves. They are much larger than bubble-generated droplets and are launched with a principally horizontal trajectory with an initial upward angle roughly equal to the wave slope. For spume generated droplets, it is clear that h scales with significant wave height (see the discussion by *Andreas* [1992] or *Fairall et al.* [1994]). While there is some interest in the details of the source distribution along and above the dominant waves, for our purposes it is sufficient to consider an area-averaged source of the simplest specification: Q_n is a delta function at the source height h so that S_n is a constant for $z < h$ (region I) and $S_n = 0$ for $z > h$ (Region II). It is critical to note that this simplified form assumes that evaporation of the droplets is negligible. We do not expect this to be valid for small droplets, but for droplets 0.1 mm and larger it is a good approximation. Mathematically we approximate the droplets produced by flow over waves as a conventional turbulent surface layer over a flat surface with droplets being continuously created at the source height.

2.2. Simple Source and Profile Relationships

[9] Turbulent transport in the surface layer is conventionally scaled with similarity theory. For example, the turbulent stress, τ, is used to define the friction velocity, u_*

$$\tau = \rho_a \overline{w'u'} = -\rho_a u_*^2 \tag{5}$$

Near a flat surface, the height dependence of the mean wind speed is (neglecting buoyancy effects) logarithmic

$$U(z) = \frac{u_*}{\kappa} \ln(z/z_o) \tag{6}$$

where $\kappa = 0.4$ is the von Karman constant and z_o the roughness length. From the vertical derivative of (6) we can relate the turbulent flux to the vertical gradient

$$\overline{w'u'} = -\kappa z u_* \frac{\partial U}{\partial z} = -K(z) \frac{\partial U}{\partial z} \tag{7}$$

where $K(z)$ is called the turbulent eddy diffusion coefficient.

[10] An eddy diffusion coefficient is also used to describe turbulent transport of passive scalars (e.g., heat, moisture) in the surface layer. In the case of droplets, the covariance terms from (4) can be combined

$$\overline{w'n'} + \overline{w_s'n'} = -K_p(z) \frac{\partial n}{\partial z} \tag{8}$$

where K_p is the eddy diffusion coefficient for droplets which combines both the w' and the w_s' covariance terms. In the case of heavy particles, the slip velocity term has an effect on the transport. The effect of the slip term is to reduce the diffusion of massive particles because their inertia prevents them from following the smaller scales of turbulence, thus reducing their diffusivity. For example, this can be approximated as [*Kepert et al.*, 1999]

$$K_p(z) = \frac{\kappa z u_*}{1 + C\left(V_g/\sigma_w\right)^2} = \kappa z u_* f_s = K(z) f_s \tag{9}$$

$C \approx 2.0$ and σ_w is the standard deviation of vertical velocity. Over the ocean (and in our wind tunnel) the surface is not flat and the flow is perturbed by waves near the surface in a region referred to as the wave boundary layer (WBL [*Edson and Fairall*, 1998]). However, (6), (8), and (9) are reasonable approximations *above* the waves and have been used successfully to simulate sea spray profiles [*Edson and Fairall*, 1994]. Flow over waves also enhances σ_w so we expect the slip factor f_s to be near 1.0 for our experimental study.

[11] Above the source region, $S_n = 0$ and (4) simplifies to

$$F_o = -K_p(z) \frac{\partial n}{\partial z} - V_g n \tag{10}$$

Because of the very strong winds relevant to our problem, we have ignored hydrostatic stability effects. For the large droplets of interest here (radius greater than about 10 μm) the two terms in (10) tend to cancel so $F_o \approx 0$. This gives a simple differential equation with a well-known [*Toba*, 1970] solution

$$n(z) = n(h) \exp\left[-\frac{V_g}{\kappa u_* f_s} \ln(z/h)\right] = n(h) \left[\frac{z}{h}\right]^{-\frac{V_g}{\kappa u_* f_s}} \tag{11}$$

In the region below the source, (4) becomes

$$F_o = -K_p(z) \frac{\partial n}{\partial z} - V_g n + S_n = 0 \tag{12}$$

This situation can also be solved analytically [*Fairall et al.*, 1990; *Hoppel et al.*, 2002] but to a good approximation the vertical gradient of n becomes negligible just below the source, so the last two terms balance. Thus, we can write

$$S_n = V_g n(h) = V_g n(z) \left[\frac{z}{h}\right]^{\frac{V_g}{\kappa u_* f_s}}, z > h \tag{13}$$

An example of size-dependent droplet profiles resulting from this simple thin layer Gaussian specification of Q_n is shown in Figure 1. The S_n profile obtained from (3) is actually an error function but for a sufficiently thin source region we can approximate that as a step function. Here we have selected the case $u_* \approx 1.6$ ms^{-1} and in Figure 1 (right) shows profiles of droplet concentration normalized by the value at source height ($n(h)V_g \approx S_n$) at three sample droplet sizes (31, 100, and 310 μm radius). For these three sizes the corresponding exponential factors, $V_g/\kappa u_*$, are 0.17, 1.03 and 3.87.

[12] Equation (13) and variations thereof form the basis of one method of estimating the surface source strength from measurements of droplet concentration over the ocean [*Fairall et al.*, 1983; *Fairall and Larsen*, 1984; *Smith and Harrison*, 1998; *Lewis and Schwartz*, 2004]. Also, (11) and (13) can be used as similarity concepts to rationalize measurements of droplet profiles done in the laboratory.

3. Droplet Source Parameterizations and Scaling Arguments

[13] In their review, *Lewis and Schwartz* [2004] discuss nine different methods to estimate the droplet source

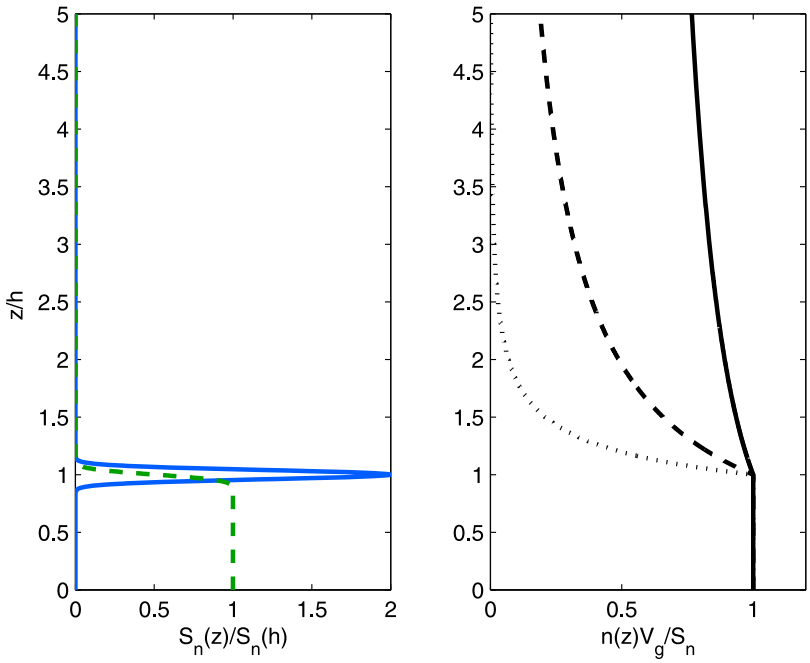

Figure 1. Sample normalized droplet profiles to illustrate relationships from section 2. (left) An example of a narrow Gaussian specification of Q_n (solid line) at source height h. The source flux term S_n (dashed line) is obtained from (3). (right) Expected normalized nonevaporating sea spray profiles computed using (13) for $z > h$ for droplets of 31 (solid line), 100 (dashed line), and 310 (dotted line) μm radius. In this case we have used $u_* = 1.6$ ms^{-1}. For $z < h$ we assume $n(z,r)$ is constant with the value $n(h,r)$.

strength. Several examples in popular use today employ regressions against wind speed of values derived with measured droplet concentrations using (13) or related versions [e.g., *Smith et al.*, 1993], from laboratory measurements of particle production from a breaking wave that is scaled to the open ocean using wind-speed-dependent whitecap coverage [e.g., *Monahan and O' Muircheartaigh*, 1980], or some hybrid of the two [*Fairall et al.*, 1994]. A simple example, the *Fairall et al.* [1994] function is represented as

$$S_n(r, U_{10}) = W(U_{10}) f_n(r) \tag{14}$$

where W is the fraction of the ocean area covered by whitecaps and $f_n(r)$ is the size distribution representing the production of a fully whitecap covered sea. The shape described by $f_n(r)$ is assumed independent of conditions. One problem with (14) is that typical formulae for the wind speed dependence of whitecaps reach saturation at wind speeds of 40 ms^{-1}. This suggests the fraction of *active* breaking might be a better variable choice, but really opens the door to pondering more fundamental processes driving the introduction of sea spray droplets into the atmosphere. The term active breaking is used to describe the spilling wave crests of breaking waves as distinct from the bubble plume associated with the dissipating remains of the active breaker (referred to as Stage A and Stage B whitecaps by *Monahan* [1989]). Spume droplet production is directly associated with active breakers while bubble-mediated spray is more closely linked with the entire bubble plume.

[14] Such source functions must be extrapolated from their regions of validity (either from laboratory to the open ocean or from lower wind speeds to hurricane wind speeds). Extrapolation based on physical scaling is usually preferred to extrapolation of regression fits, but a physical scaling for droplet production based on the fundamental dynamics of the system has yet to be developed. Traditional scaling methods, such as dimensional analysis, require identification of the relevant independent parameters, a tricky business in very complicated systems. While complete detail on S_n is not required, for most purposes information is needed on the droplet size at the volume distribution peak, total mass flux, size dependence of the fall off at the upper end of the spectrum, and how the overall distribution scales with forcing conditions. In particular, fundamental forcing parameters are preferred (as opposed to just a crude wind speed dependence) so we can reliably extrapolate for hurricane conditions where direct confirmation of the source term is experimentally problematical.

[15] *Andreas* [2002] argued that the energy required to create droplets from flat water came from the wind energy flux into the ocean (scaling roughly was wind speed or friction velocity to the third power). This energy input is usually balanced by wave breaking, giving a natural connection to whitecap fraction. In the spirit of (14), this implies

$$S_n(r, u_*) \approx u_*^3 f_n(r) \tag{15a}$$

$$S_n(r, P_b) \approx P_b f_n(r) \tag{15b}$$

where P_b is the energy dissipated by breaking waves. Note that (15a) requires assumptions about the balance of wind input and the breaking of waves while (15b) does not. *Bye and Jenkins* [2006] made theoretical arguments that about 25% of energy going to the wavefield was used to create sea spray.

[16] *Anguelova et al.* [1999] analyzed wind tunnel simulations and argued that droplet production scaled with the mean length of breaking waves per unit area, Λ, which they found goes approximately as wind speed cubed

$$S_n(r,\Lambda) \approx \Lambda f_n(r) \tag{16}$$

A similar but more complicated scaling was developed by *Kudryavtsev* [2006], who convolved a band-limited mean breaking length with energy production arguments similar to (15a). This led to a source function proportional to the fifth power of u_*. *Emanuel* [2003] offered a scale analysis of spray and found that the criteria for the lofting of spray by turbulence was characterized by the scaling parameter

$$R_u^{1/4} = \frac{u*}{(\sigma\, g)^{1/4}} \tag{17}$$

where σ is water surface tension divided by density and g the acceleration of gravity. The thickness of the droplet/bubble layer is related to a Reynolds number on the basis of the gradient of fluid density. *Zhao et al.* [2006] found that spume production data were scaled consistently by a wind-sea Reynolds number ($\frac{u_*^3 W_A}{g\nu}$ where $W_A = c_p/u_*$ is the wave age with c_p the wave phase speed and ν the kinematic viscosity), while simple wind speed scaling failed to collapse the data.

[17] Droplet size scaling has been discussed by *Hinze* [1955] who suggested that the upper limit of droplet size was determined by the breakup of droplets by small-scale turbulent shear. This suggests that the maximum droplet size should decrease with increasing forcing

$$r_m \approx \left(\sigma^3/\varepsilon^2\right)^{1/5} \tag{18}$$

where ε is the rate of dissipation of turbulent kinetic energy. Near the interface, dissipation scales as u_*^4/ν, so r_m would scale as $[\sigma^3\nu^2/u_*^8]^{1/5}$. *Bye and Jenkins* [2006] offer a different analysis, suggesting that droplets will be directly subjected to the mean wind speed at 10 m height. This leads to the r_m scaling as σ/u_*^2. *Newell and Zakharov* [1992] discussed the balance of energy inputs and the breakdown of the surface into droplets and bubbles, a process that begins when the energy input to waves, P, exceeds a threshold

$$P_0 = (\sigma\, g)^{3/4} \tag{19}$$

[18] Note that, because P scales roughly as u_*^3, (17) is essentially equivalent to (19). *Newell and Zakharov* discuss the size scales in terms of capillary wave number spectra and the thickness of the bubble/droplet layer. *Garrett et al.* [2000] discuss the relationship of oceanic bubble size spectra and forcing in terms of the dissipation rate. Unlike sea spray, the size of bubbles changes with pressure, so analogies with droplet spectra are not useful. The Kolmogorov microscale, η_k, is a natural size scale limit for turbulent processes at the interface

$$\eta_k = \left(\frac{\nu^3}{\varepsilon}\right)^{1/4} \tag{20}$$

Spume production is a special case because droplets produced at the interface near the peak of a breaking wave are easily blown off the top of the wave by turbulent wind gusts [*Andreas*, 2004]. In fact, this is probably the only way the larger droplets can influence the atmosphere. Thus, the probability that a droplet will be launched into the turbulent flow and spend a significant time with an airborne trajectory is related to the slope of its trajectory compared to the slope of the wave. This can be characterized by the scaling parameter

$$R_{slope} = \frac{V_g/U_t}{h/\lambda} \tag{21}$$

where U_t represents the mean wind speed near the wave top and λ the wavelength.

4. SPANDEX Details

[19] SPANDEX is an exploratory water-wind tunnel study to investigate the scaling of the production of large (spume) droplets associated with wind/stress interactions with actively breaking waves. The obvious experimental tasks are to characterize the flux of sea spray over some range of wind/stress/wave forcing. In section 2 we used idealized physics to argue that the droplet flux as a function of size can be related to profiles of mean droplet concentration, the friction velocity, and significant wave height. Three different optic systems are used: a droplet imaging probe to measure drop concentrations in the 0.025 to 1.55 mm diameter range, a phase Doppler system that measures both droplet concentration (for droplets of about 4–75 μm diameter) and planar motion vector, and a high-speed video system. Friction velocity was estimated from pitot-static (PS) wind gradient measurements, and wave properties were measured with capacitance wire wave gauges. From these variables we can estimate the total suspended droplet mass and the droplet flux as realized at wave top. We are focusing on the large spume droplets which are known to lose only a few percent of their mass before reimpacting the surface, so for simplicity we neglect evaporation effects. This is a poor approximation for droplets on the order of 10 μm radius, but relieves us of the experimental complication of controlling or monitoring profiles of temperature and humidity in the tunnel. To assess the evaporation issue, we study spray with both fresh and salty water (droplets near seawater salinity will only lose no more than about half their diameter through evaporation).

[20] The forcing is characterized by wind speed, friction velocity, significant wave height, and wave period. To vary the forcing, we used three different wind speeds and waves were generated with a paddle system. The lowest wind speed was near the threshold for significant spume droplet

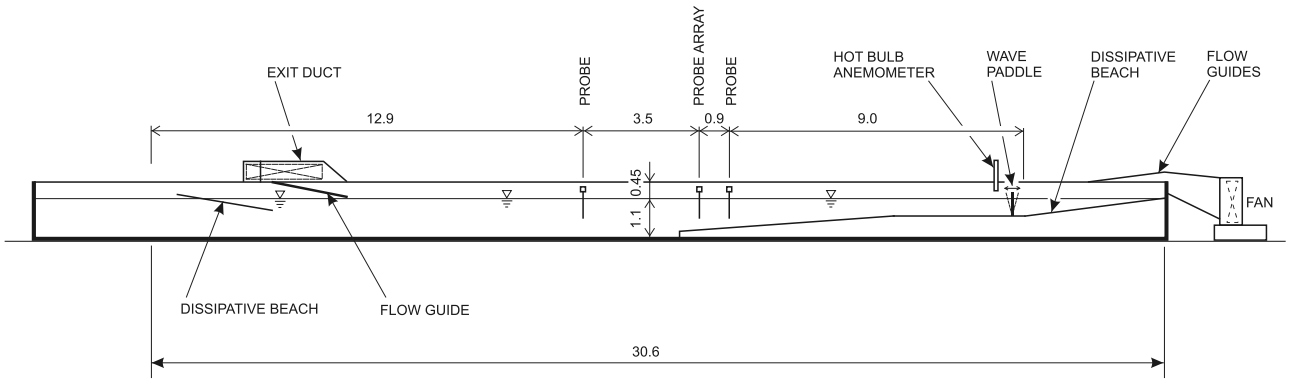

Figure 2. Schematic of wind-wave flume used in this study. All dimensions are in meters.

production in the tunnel; the maximum was the upper limit of the fan. From the discussion in section 3 it is clear that these parameters may not be fundamental, so we seek some additional index of energy flux to breaking waves. This turns out to be amazingly problematical, so we chose to use the small-scale disturbance energy (i.e., high-pass filtered water surface displacements) as a proxy for P_b. In the remainder of this section we discuss the details; discussion of the wave disturbance analysis is given in Appendix A.

4.1. Wind-Wave Tunnel and Setup

[21] Detailed observations of spray flux and the underlying breaking waves were made in a wind-wave tank at the Water Research Laboratory. This facility is 30 m long, 0.9 m wide, and 1.55 m high, and is shown schematically in Figure 2. Monochromatic waves of small steepness were initiated by an adjustable frequency paddle wave maker, located approximately 3.5 m downwind of the fan just below a large speed controllable fan, which could generate wind speeds typical of severe storms in the air channel above the water. At its downwind end, the wave tank has a dissipating beach and a duct to discharge the spray outside the laboratory.

[22] During these investigations, water depth in the tank was maintained at two levels. For most of the experiments, the water depth was 1.10 m with an air channel height of 0.45 m. The maximum wind speed achievable in the facility in this configuration was 16.7 ms^{-1}. To maximize wind forcing for one test condition, the water level was raised by 0.05 m thereby providing a wind speed of 17.8 ms^{-1} in the air channel. The strong wind-forcing rapidly amplified the paddle-generated waves, producing a train of heavily breaking waves within a few meters of the paddle. An image of a typical breaking wave is shown in Figure 3. In an effort to maintain a consistency of waveform and energy flux from the wind to the waves, low steepness waves were generated at the paddle. Under the action of the wind, these waves grew in amplitude along the tank but retained their underlying frequency. The fetch where breaking began was set to be similar for each of the wind and wave conditions observed. This was achieved by adjusting the steepness of the initial wave train produced by the paddle. Detailed measurements were undertaken at an observation point located approximately 10 m from the paddle.

[23] During the course of the experiments, the water salinity was adjusted by stirring in salt to the fresh water from the supply. The salinity was increased from fresh water to 24 ppt (parts per thousand) incrementally by 6 ppt, and spray, wave and wind measurements were made for each salinity.

4.2. Instruments

4.2.1. Concentration Profiles Droplet Probe

[24] The SPANDEX study used the Cloud Imaging Probe, concentration profiles (CIP) manufactured by Droplet Measurement Technologies (DMT) in Boulder, CO, USA. The CIP is a technology based on a linear array of 64 light detecting diodes [*Knollenberg*, 1970]. As it transits the beam, the particle casts a shadow across the array and the size is deduced from the number of diodes that are occulted. This technique is a fairly mature technology and numerous papers have been written on deriving accurate droplet size information [e.g., *Baumgardner and Korolev*, 1997]. Droplets are sized from 25 to 1550 μm diameter in 62 equally spaced 25 μm diameter bins. Droplet number

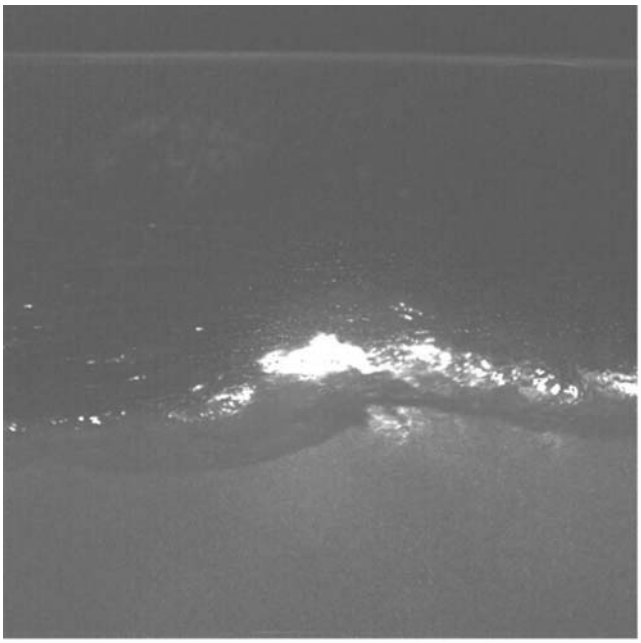

Figure 3. Typical high-speed video image showing spray droplets shed by a breaking wave, captured at 200 Hz.

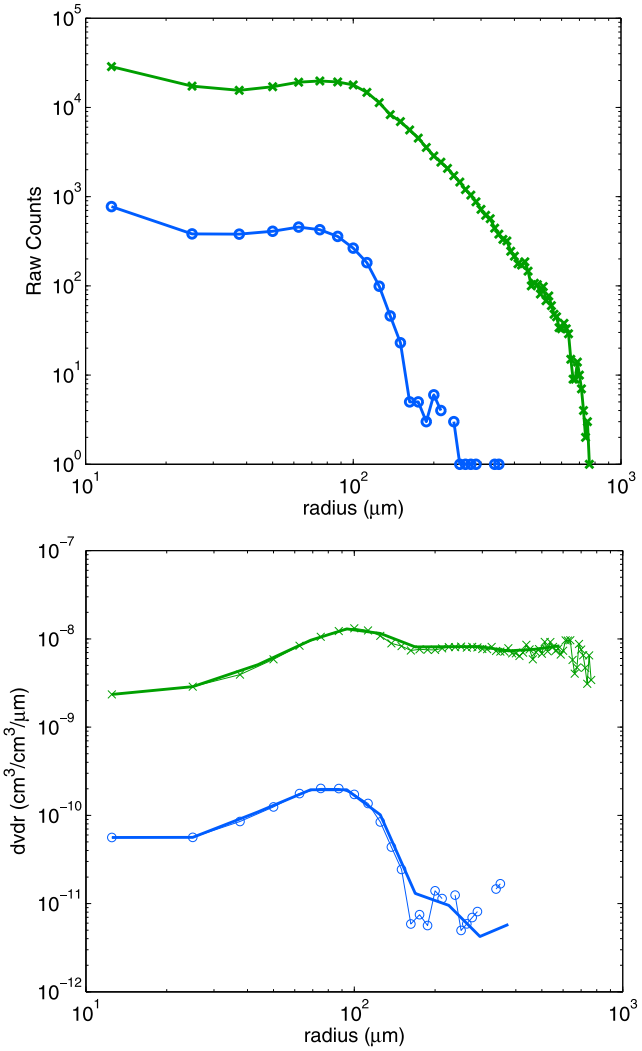

Figure 4. Examples of raw and smoothed volume spectra for two cases (crosses are 12.5 cm height with strong forcing and circles are 24.5 cm with weak forcing). The (top) raw counts and (bottom) volume spectra are shown. The total sample at 24.5 cm was 29 min long but with weaker forcing no droplets were counted for radius greater than 350 μm.

concentrations are computed from droplet counts in each size bin using the expression

$$n(r) = \frac{Total\ Counts(r)}{a(r)U(z)drdt} \tag{22}$$

where $U(z)$ is the flow speed through the sample region in cm s^{-1}, dt the sample time interval, dr the sample radius bin width (12.5 μm), and $a(r)$ the size-dependent sample cross-sectional area in cm^2 (provided by the manufacturer). The sample area (in other words, the counting sensitivity of the device) depends on particle size through the effective depth of field (which increases with increasing particle size up to 325 μm diameter) and the requirement that both edges of the particle's shadow must be resolved for it to be unambiguously sized (which causes the sample area to decrease linearly as particle size increases). This declining sensitivity to larger particles implies the CIP is not ideal for defining the radius dependence of concentrations for the larger particle sizes (see below).

[25] The CIP is set to sample at 1 s time resolution. For the analysis presented in this paper, the counts were totaled for each run and a single spectrum was computed. A smoothing routine was run to simplify the spectrum. Examples of raw counts and smoothed volume spectra from runs on 6 and 7 February for two cases (12.5 cm height above mean water level with strong forcing and 24.5 cm with weak forcing) are shown in Figure 4. The total sample at 24.5 cm height was 29 min long but no droplets were counted for radius greater than 350 μm. However, between 250 and 350 μm radius zero and nonzero counts were intermixed. The smoothing routine is a simple mechanism to estimate the number spectrum in this size region. Note that for strong forcing the number of counts drops below 100 at a radius of about 500 μm and then plummets rapidly to a single count at the largest size even though the volume concentration is approximately constant with increasing radius. Thus, in these conditions the droplet spectra are not well sampled for radii exceeding about 600 μm.

[26] For any spectrum we can compute an estimate of the suspended droplet mass at a given height

$$M(z) = \frac{4\pi\rho_w}{3}\int n(z,r)r^3dr = \rho_w\int V(r)dr \tag{23}$$

where ρ_w is the density of seawater water and $V(r)$ the volume concentration. Similarly, we can compute an estimate of the droplet mass flux realized at the source height h

$$F_m\frac{4\pi\rho_w}{3}\int\left[V_g n(z,r)\exp\left[\frac{V_g(r)}{\kappa u* f_s}\ln(z/h)\right]\right]r^3dr \tag{24}$$

For measurements near wave crests, the mass and mass flux scale as the third and fourth moments of the measured spectrum. As z increases, the weight of larger sizes increases further making estimates of mass and mass flux estimates very sensitive to poor counting statistics.

4.2.2. Wind Measurements

[27] A reference wind speed in the air cavity U_{ref} was monitored using a hot bulb anemometer mounted from the roof within the air cavity in the upwind section of the tank (Figure 2). The anemometer was inserted only 0.125 m into the air cavity to minimize any spray influence. The atmospheric friction velocity was determined by measuring the near-surface logarithmic boundary layer profile in the air for each wind speed condition. These were taken at the point of spray measurement within the tank. The velocity measurements were made using a small pitot-static tube with its pressure ports connected to a high-resolution Barocel micromanometer, whose output was connected to a data acquisition computer sampling at 100 Hz.

[28] The measurements of wind speed were extremely difficult to accomplish, particularly close to the interface. Spray in the air tended to contaminate the small (~0.5 mm) Pitot orifices and distort the velocity measurements. However, this was easy to detect as, once contaminated, velocity

Table 1. Summary of Measured Airflow Profile and Wave Parameters

		Fresh Water		24 ppt Salinity		Wave	
Forcing	Wind Speed, U_{ref} (ms^{-1})	u_* (ms^{-1})	z_0 (mm)	u_* (ms^{-1})	z_0 (mm)	Amplitude (mm)	Frequency (Hz)
Weak	14.5	1.35	3.68	1.06	1.45	47	1.62
Nominal	16.7	1.44	3.34	1.64	4.04	65	1.36
Strong	17.8	1.64	3.12	1.78	5.25	48	1.36

fluctuations would become strongly damped and the mean velocity would drift consistently.

[29] To ensure that the velocities were not affected by water contamination of the Pitot tube, the following method of measurement was adopted:

[30] 1. The Barocel was disconnected and the PS tube was cleared of any water droplets by applying a substantial back pressure.

[31] 2. The Barocel was reconnected and the data acquisition system was reset. The purging process involved a delay of only a few seconds.

[32] 3. The data acquisition system provided continuous output of the running velocity averaged over 0.5 s, as well as the mean velocity since the last reset.

[33] 4. The data acquisition system outputs were monitored for damping of fluctuating velocities or drifting mean velocities. The average velocity was recorded over a fixed measurement interval (10 or 20 s) if there was no evidence of the measurement being contaminated by water in the PS tube.

[34] Steps 1–4 were repeated for a given elevation within the logarithmic velocity distribution region until a stable mean value was achieved. The results of the friction velocity measurements are shown in Table 1. Supporting spray measurements indicate that their concentrations remained strictly less than 3 g^{-3}. As a cubic meter of air weighs approximately 1.2 kg, the effect of the spray on the momentum flux is less than 0.3%.

4.2.3. Wave Conditions and Measurements

[35] Two wave paddle frequencies were used during these observations (1.36 Hz and 1.62 Hz). The wave generator initiated a train of narrow bandwidth, low steepness waves, which rapidly amplified under the action of the very strong overlying wind. The waves grew to breaking, with almost every wave breaking actively as it passed the observing station about 10 m down wind of the wave paddle. Strong modulation of the wave height accompanied the very frequent breaking. In fact, for the highest wind speed (17.8 ms^{-1}), we noted that the average wave height was attenuated to a level below the mean height of the waves forced by the 16.7 ms^{-1} winds. The measured wave parameters at the observation site are shown in Table 1. The corresponding phase speeds c_p were estimated using the linear dispersion relation $c_p = g/(2\pi f_p)$, where f_p is the paddle frequency in Hz. During this investigation, water surface elevations were monitored using two types of wave gauges. For redundancy, a four wave probe array with fine ($\sim$200 μm diameter) wire filaments was installed at the observation point. Each gauge had a range of approximately 200 mm. Two additional wave wire probes 400 mm in length with filaments constructed of Teflon-coated wire were located upstream and downstream of the wave probe array (see Figure 2).

[36] The wave probes were calibrated regularly, and over the period of our experiments showed repeatability in their gain of better than 2% in fresh water. The calibration was also undertaken in water with a salinity of approximately 25 ppt. It was found that any shifts in gain response were within the 2% variation band observed in fresh water. In collecting the wave data, a very high sample rate was used in order to resolve the high-frequency fluctuations in the free surface elevation in the breaking regions, at the same time measuring the properties of the underlying dominant (breaking) waves. For this, water surface elevation measurements of the wave probes were recorded at a frequency of 2322 Hz per channel by a computer with an A/D converter and stored for subsequent processing. Special data processing was implemented subsequently to characterize the high-frequency breaking zone disturbance energy distribution over the dominant breaking waves.

4.2.4. High-Speed Videocamera

[37] A Phantom 4 (http://www.photosonics.com/phantom-hd_cam.htm) high-speed video camera system was used to investigate details of the process of water droplet ejection locally from the wavy water surface. The video camera was set up to look through the glass tank sidewall and view droplets ejected within a collimated light sheet projected from above along the tank centerline. A rudimentary light sheet approximately 10 mm wide was formed using a bank of three 1500 W lights illuminating a strip approximately 1200 mm long and 250 mm from the glass tank wall. The geometry of the illuminated region was determined using a calibrated scale located within the light sheet. For the data gathered in this study, a frame rate of 200 Hz was chosen. A sample of one of these high-speed video images is shown in Figure 3. While it may have been possible to extract quantitative kinematic data on droplet sizes and velocities from this imagery, we were not set up for such quantitative image analysis. Instead, we chose to use the imagery to characterize the key qualitative features of the droplet ejection process. These are summarized below in section 5.2.

4.2.5. Phase Doppler Anemometer

[38] Droplet sizes and velocities were measured using a Laser Phase Doppler Particle Analyzer (TSI Inc., St. Paul, Minnesota). The LPDPA, or phase Doppler anemometer (PDA), was configured to measure droplets with a minimum radius of 5 μm and a maximum radius of 150 μm with a radius bin width of approximated 0.5 μm. Detailed discussions of the operational principles of a PDA are available elsewhere [*Bauckhage*, 1988]. Briefly, the PDA measured droplet radius r, streamwise velocity, U_x, and vertical velocity, U_z, of droplets at a single location determined by the intersection of four laser beams. The intersection volume of the beams was located 0.2 m from the sidewall of the wind tunnel and the instrument was mounted on a single-axis traverse allowing height profiling of droplet

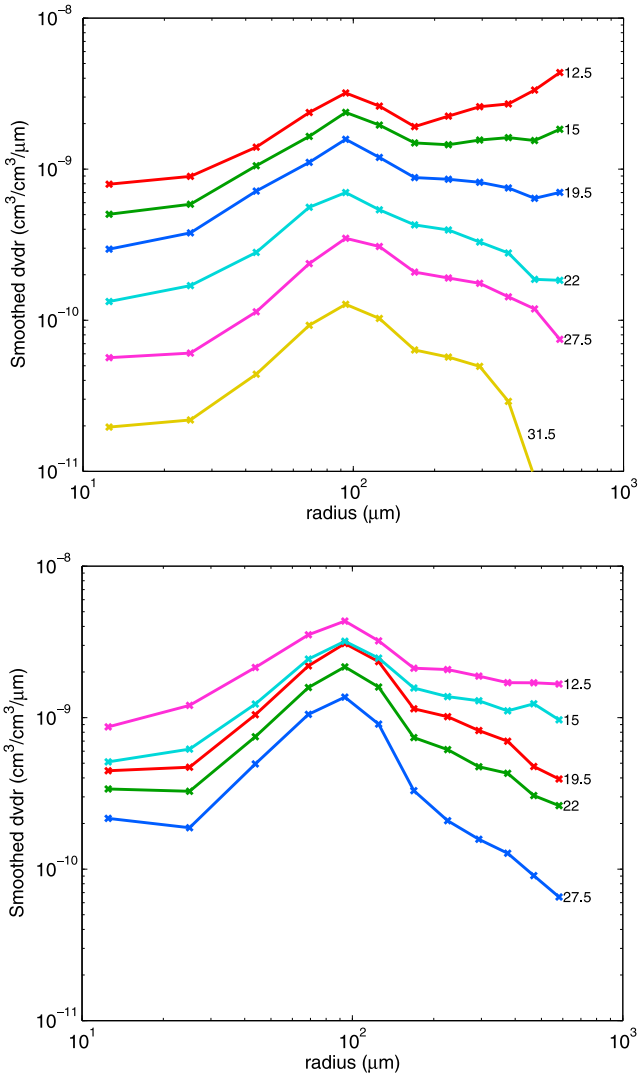

Figure 5. Sample droplet volume size spectra are shown at a nominal forcing condition for (top) fresh water and (bottom) water with salinity of 24 ppt. The height of the measurement (cm) above the mean surface is indicated at the side of the curve.

populations. In these experiments, droplets were measured at heights of 10, 15, and 20 cm above mean water level (MWL) for fresh water and 12.5, 15, and 20 cm above MWL for 24 ppt saltwater.

[39] A capacitance wire wave height gauge was positioned 1 cm downwind and 5 cm laterally toward center of the wind tunnel from the PDA measurement volume. The output from the wave gauge was digitized concurrently with the PDA data collection so that instantaneous water surface elevation was recorded along with diameter and velocity for each droplet. This allowed droplet velocities to be correlated with wave phase.

[40] The sample volume of the PDA was on order of 1×10^{-5} cm^3 which meant that even with the high overall droplet flux in the wind-wave tunnel, data rates for the PDA using spray droplets were on average 0.5 Hz. This required sample times of 1800 s for the PDA in order to acquire enough spray droplets for reliable statistics on droplet diameters and velocities. In general, the low data rate from the PDA, caused in part by droplets accumulating on the inside window of the wind tunnel, prevented accurate estimation of droplet number concentrations (number of particles per unit volume per increment of radius). However, in the cases where the comparison could be made, the PDA values for $n(r)$ were consistent with those measured by the CIP, suggesting that the PDA was accurately sizing droplets.

[41] Measurements were also made using seeded water droplets produced by a high-pressure paint sprayer located 3 m upwind of the PDA measurement volume. The sprayer was oriented so that the droplets were injected perpendicularly to the main wind flow in the tunnel with no vertical velocity. The measurements with seeded droplets were always made as the final measurements under each condition so that there was little possibility of their contaminating the CIP data set or PDA spray droplet data set. The seeded particles produced data rates of approximately 100 Hz, and were used to study flow patterns in the tunnel that were responsible for producing the spray droplets. Vertical profiles of U_x measured using the seeded droplets showed that for $U_{ref} = 16.7$ ms^{-1}, the PDA data for U_x resulted in a u_* for freshwater of 1.67 ms^{-1} and u_* for 24 ppt saltwater of 1.71 ms^{-1}, which is in good agreement with the data in Table 1. This agreement demonstrates that the PDA provided reasonable data for droplet velocities in the wind-wave tunnel.

5. Results

5.1. Droplet Concentration Profiles

[42] One goal of SPANDEX was to examine the validity of the simplified scaling model of droplet concentration profiles. This was done by measuring concentrations at several heights above mean water for a fixed forcing. Sample droplet volume size spectra are shown at a nominal forcing condition ($u_* \approx 1.6$ ms^{-1} and $h \approx 0.11$ m) for fresh water (Figure 5 (top)) and for water with salinity of 24 ppt (Figure 5 (bottom)). The spectrum at each height, $n(r,z)$, can be converted to an effective concentration at the source height, $n(r,h)$, using (11). The results are shown in Figure 6. If the assumptions used to derive (11) are valid, then we expect all spectra to collapse on a single line. Contrast the spread of the spectra taken at different heights shown in Figure 5 with the near collapse to similar values shown in Figure 6. It is clear that droplet evaporation is playing a significant role in deviations from (11). The range of normalized concentrations for the smaller particles is about 1.5 orders of magnitude for freshwater but is only 0.5 orders of magnitude for the saline water. This is consistent with the r^{-2} scaling of the normalized droplet evaporation rate, $\dot{r}/r$, and with the fact that saline droplets do not completely evaporate but approach an equilibrium size on he basis of their salt content and the local relative humidity [*Fairall et al.*, 1990]. The salinity effect also explains why the volume spectra for freshwater droplets are still increasing with size out to 0.8 mm radius while the saline droplets level off at about 0.1 mm radius. One interesting feature of the normalized spectra is they are relatively constant with increasing radius above 0.1 mm radius and show no tendency to turn down at the larger sizes. This suggests that the total mass in the distribution is not well constrained and the mass flux is poorly constrained. This might also be an evapora-

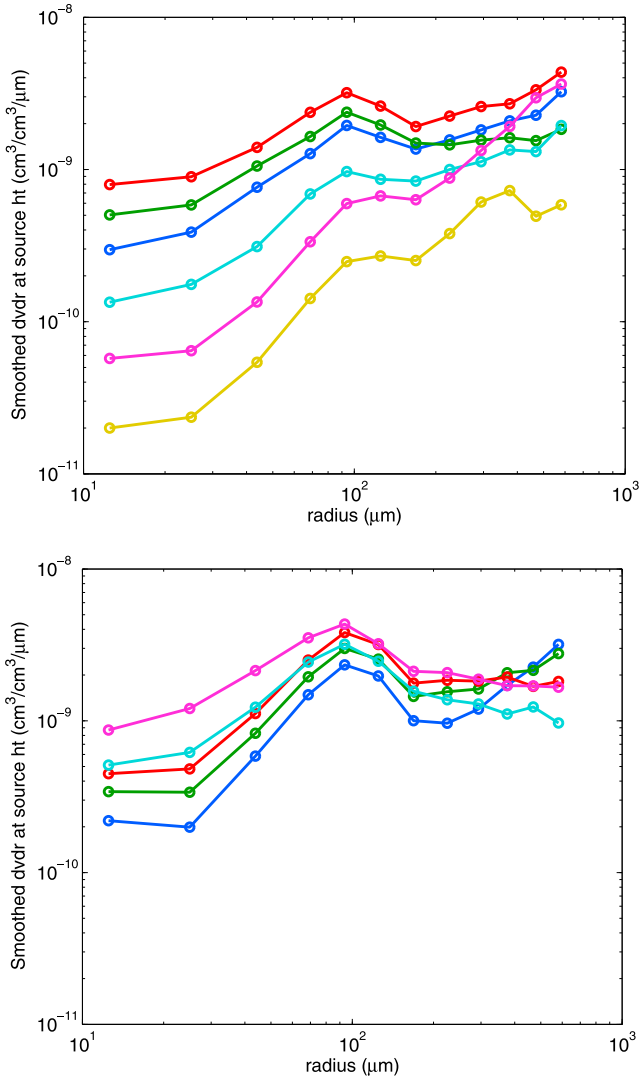

Figure 6. As in Figure 5 except the spectrum at each height $n(z,r)$ have been converted to an effective concentration at the source height $n(h,r)$ using (11).

tion effect, a measurement artifact, or some other weakness in our assumptions. For example, in reality the source is not a delta function at h but has some vertical distribution; and this difference will complicate the conversion to the normalized concentration, particularly for samples further from the surface (note the deviation of estimates for large droplets from the highest profile). Another possible factor is the ballistic trajectory of the largest droplets allows them to occasionally be nondiffusively transported to well above wave top (this is easily verified visually in the tunnel). However, the most likely candidate is counts at the larger sizes are caused by two smaller droplets passing through the sample volume at the same time. In that case, the CIP software would indicate a single drop with a size equal to the sum of the sizes of the two drops plus the distance between them (i.e., the outer edges of each drop would be computed as the outer edge of a fictitious single drop).

[43] The dependence of droplet concentration on the forcing of the system is illustrated by plotting normalized concentrations for different wind-wave conditions. To simplify the plots and reduce the sensitivity of (11), we show only the normalized concentrations from near the surface (z = 12.5 and 15.0 cm). Normalized spectra are shown for three levels of wind forcing for freshwater (Figure 7 (top)) and saline water (Figure 7 (bottom)). On this scale, fresh and saline water droplet spectra are surprisingly similar, suggesting there is little difference in the production by the spume mechanism. The large droplet volume concentrations at source height increased from about 4×10^{-10} to 7×10^{-9} as u_* increased from 1.2 to 1.6 to 1.8 ms^{-1}. The increase from 1.2 to 1.6 is consistent with $u_*^{4.5}$ but the exponent for the increase from 1.6 to 1.8 is 13. This is clear evidence that u_* is not the sole scaling parameter for the source strength. Total near-surface droplet mass and the estimated mass flux are shown in Figure 8. The parameterizations of *Kudryavtsev* [2006], *Fairall et al.* [1994], and a

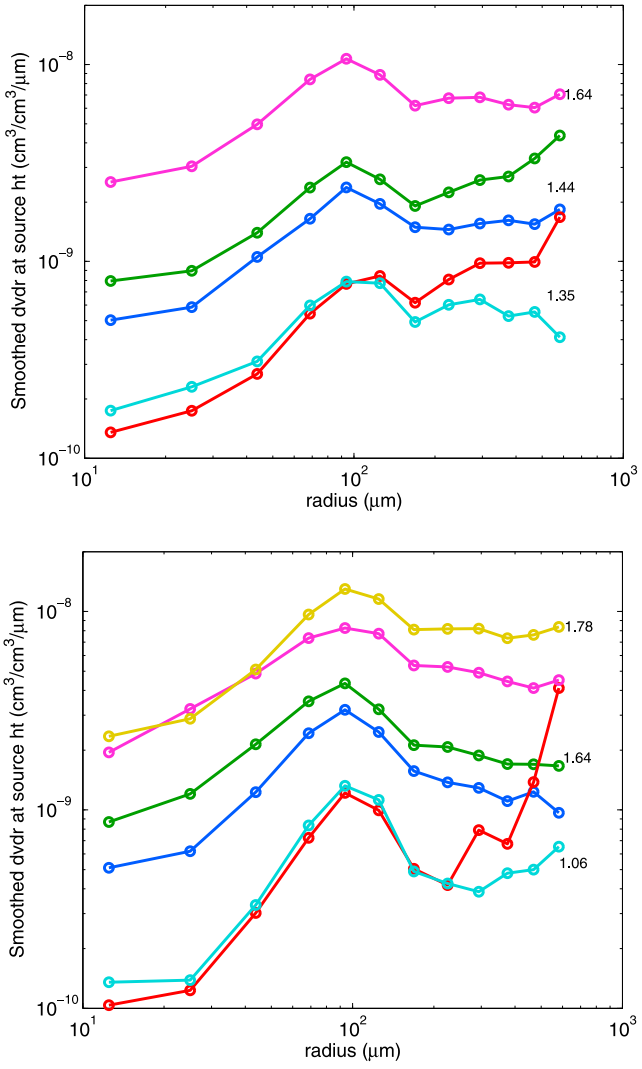

Figure 7. Normalized volume concentration spectra (volume of water per volume of air per radius increment) from near the surface (z = 12.5 and 15.0 cm). Normalized spectra are shown in pairs for three forcings for (top) freshwater and (bottom) saline water. The forcing is shown by the value of u_* at the right-hand edge of the line. The curve for z = 15 cm is missing for the fresh water maximum forcing case.

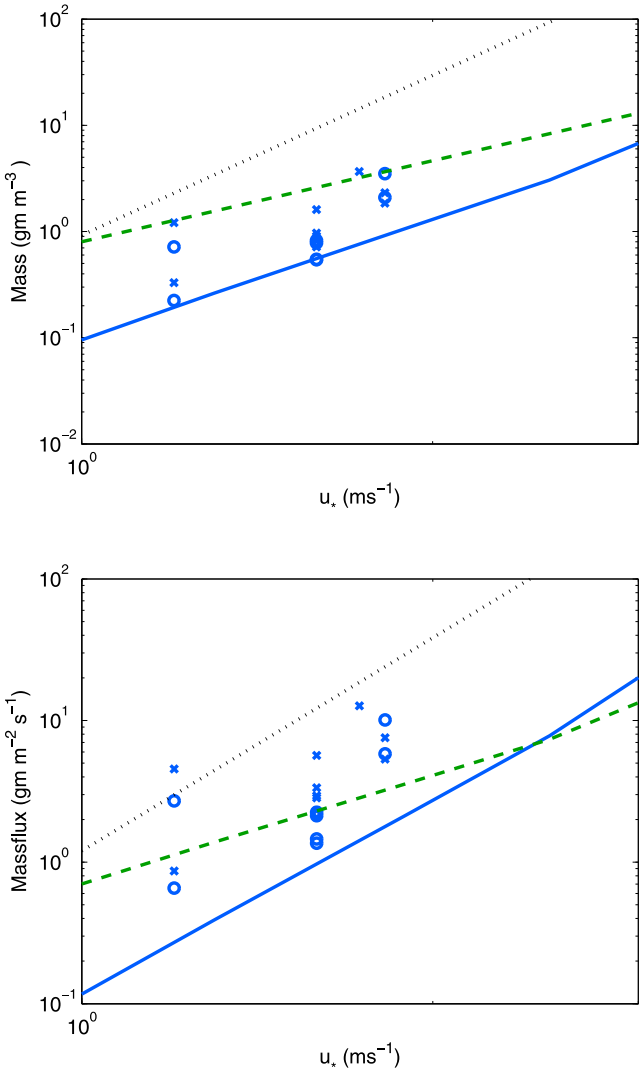

Figure 8. Total near-surface droplet mass and the estimated mass flux near the surface as a function of u_* for the 24 ppt salinity cases. The SPANDEX data are indicated by symbols (z = 12.5 and 15.0 cm as circles and z > 15 cm but z < 30 cm as crosses). The dotted line represents a parameterization by *Kudryavtsev* [2006], the dashed line represents the parameterization of *Fairall et al.* [1994], and the solid line represents a recent update of that parameterization obtained from a physically based model (Fairall and Banner, manuscript in preparation, 2009).

recent update of that parameterization obtained from a physically based model (C. W. Fairall and M. L. Banner, Sea-spray and air-sea interaction at hurricane wind speeds. Part I: A physically based sea-spray droplet spectrum source parameterization, manuscript in preparation, 2009, available at ftp://ftp.etl.noaa.gov/user/cfairall/onr_droplet/parameterization/spray_drop_param_3.doc) are shown for reference. The Fairall and Banner (manuscript in preparation, 2009) parameterization is described briefly in Appendix B. For *Kudryavtsev* [2006] we have taken the spume droplet area flux, $F_A = 0.02u_*^5$, from his Figure 7 assuming droplets of 180 μm radius. For *Fairall et al.* [1994], u_* was converted to U_{10} via (6) and that was used directly in the parameterization. There is no reason to expect these parameterizations to be consistent with the wind tunnel results, but in this case they are fairly close. The large scatter in the results for the weaker forcing is associated with the tendency for the normalized spectra to turn up for large droplets as discussed above. Also, the tendency for higher values to be associated with data further from the surface suggests that (11) is overcorrecting the height dependence.

5.2. PDA Measurements of Droplet Velocity Statistics/Profiles

[44] Water surface elevation measured by the wave wire gauge was used to separate both spray and seeded droplets into two categories on the basis of water surface elevation: those measured over the wave crests (defined as droplets for which the water surface elevation was 2 cm and greater, relative to MWL); and those measured over wave troughs (defined as droplets for which the water surface elevation was −4 cm or less, relative to MWL). Figure 9 shows vertical profiles of the horizontal along-stream velocity, U_x, for fresh water spray droplets compared to U_x measured using the injected seeded particles where the data have been sorted into U_x measured over wave crests and U_x measured over troughs. As expected, regardless of whether spray droplets or seeded droplets were used, U_x measured over both crests and troughs decreased with decreasing measurement height. The spray droplet and seeded droplet data also show the common feature that for the lowest height measured, U_x measured over the wave crests is less than U_x measured over wave troughs. However, there are two key points to be made concerning the data shown in Figure 9.

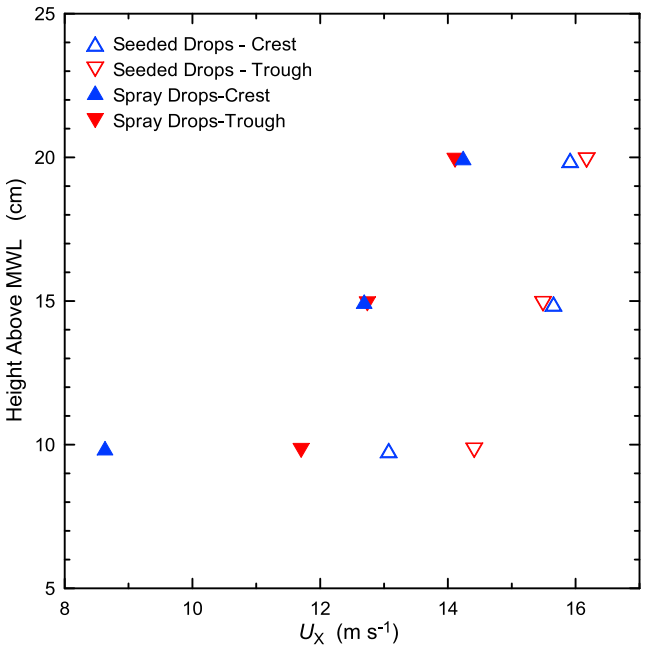

Figure 9. Average horizontal along-stream droplet velocity U_x for spray droplets generated from the breaking waves and seeded droplets injected into the flow using a high-pressure paint sprayer. The spray droplets and the seeded droplets have been sorted into two bins as those measured over the tops of wave crests and those measured over wave troughs.

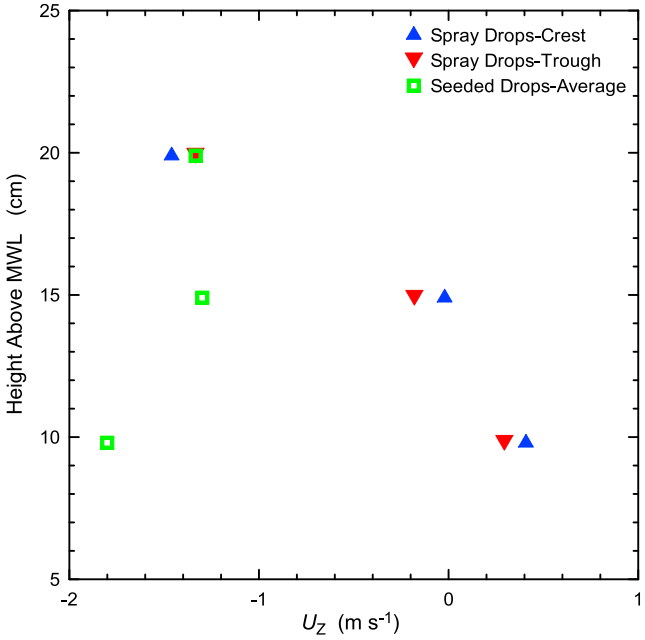

Figure 10. Average vertical droplet velocity U_z for spray droplets generated from the breaking waves and seeded droplets injected into the flow using a high-pressure paint sprayer. The spray droplets have been sorted into two bins as those measured over the tops of wave crests and those measured over wave troughs. The seeded drops are averaged over all wave phases.

[45] The first point is that U_x for spray droplets (i.e., droplets generated by the breaking waves) are less than U_x for the seeded particles at all heights regardless of whether the droplet velocities are measured over troughs or crests. Because there was good agreement between U_x measured using the hot bulb anemometer and u_* determined from the Pitot tube profiles with U_x and u_* derived from the PDA measurements of the seeded droplets, it is reasonable to assume that U_x for the seeded particles represents an accurate measurement of the local free stream wind velocity. Therefore, the data in Figure 9 suggest that the spray droplets had not accelerated to the mean free stream wind velocity when they were sampled by the PDA.

[46] A noteworthy finding is that for the spray droplets, the near-surface difference between U_x measured over the wave crests and troughs is much greater than the difference in U_x for the seeded droplets. Although the crest-trough difference in U_x for the seeded drops is likely to be real and caused by increased drag at the water surface, the larger crest-trough difference in U_x for the spray drops might be controlled by somewhat difference physics. The video measurements show that droplets are generated on the wave crests, and therefore the droplets measured over the wave crests are in general younger than droplets measured over the troughs. Therefore, the larger difference in U_x reflects the fact that at low heights above the water surface, the younger droplets have had less time to accelerate than the older droplets over the troughs. Age becomes less important in determining U_x as the spray droplets rise above the water surface, as is shown in the data by there being no difference in the velocity for heights greater than 15 cm above MWL.

[47] Figure 10 shows the vertical profile in U_z measured for spray droplets over wave crests and troughs along with the vertical profile in U_z averaged over all data for the seeded droplets. At a height of 20 cm above the MWL, there is no difference between U_z measured for spray drops over crests, U_z measured for spray drops over wave troughs, or U_z measured for the seeded drops. This suggests that at a height of 20 cm, the droplets are above the source acceleration region, which is supported by the plots of size-segregated droplet concentrations measured by the CIP.

[48] The value of U_z for the spray droplets is positive at the lowest elevation measured regardless of wave phase, near zero at a height of 15 cm, and negative at a height of 20 cm. Because the seeded droplets show a large average negative vertical velocity at all three elevations, a positive U_z for the spray droplets implies they are moving quite rapidly upward until they reach a height of 20 cm. It is not clear why on average the seeded drops and spray drops at 20 cm have such large downward velocities associated with them. It is possible these motions are caused by secondary flows in the wind tunnel.

[49] Overall, the PDA data support the conclusions regarding droplet formation from the video data that droplets are generated from near the breaking wave crests, launched with upward trajectories, and rapidly accelerate to the free streamflow velocity. The actual magnitude of the mean spray droplet slip velocities is also interesting. *Andreas* [2004] computed horizontal acceleration times of spray droplets as a function of size and wind speed. His calculations suggest that a 100 μm radius droplet would accelerate to within a few ms^{-1} of the mean wind speed at 0.1 m above mean water in about 0.05 s. Thus, the observed slip velocities seem large, implying that we are seeing the droplets almost at formation or perhaps the droplets tend to be preferentially occupying air that is moving more slowly (e.g., updrafts). The updraft hypothesis is consistent with the mean vertical slip velocity also. These results are an interesting complement to the wind tunnel study of *Koga* [1986] who used particle imaging techniques to examine velocity deficits of much larger droplets (1.2, 3.5, and 5.5 mm). These particles had horizontal velocities about half the mean flow and velocities on the upslope of the wave were considerably larger than the downslope and trough. Thus the mm-size droplets either have not had time to reach the mean flow speed or are occurring preferentially in slower moving air; the difference in upslope and downslope speeds is also puzzling.

5.3. Breaking Wave Statistics

[50] The wind-forcing conditions in our experiments were very strong ($U/c_p \sim 14.4$ to 15.5). These are certainly well beyond wind-forcing conditions for the dominant waves in a hurricane, but are likely to be typical of forcing levels of intermediate-scale waves in such conditions. In any event, we observed through careful visual monitoring that for each of the reference wind/wave conditions, every crest was breaking as it passed our observation point. Under less strongly forced conditions, the results would need to be conditioned by a breaking probability multiplier.

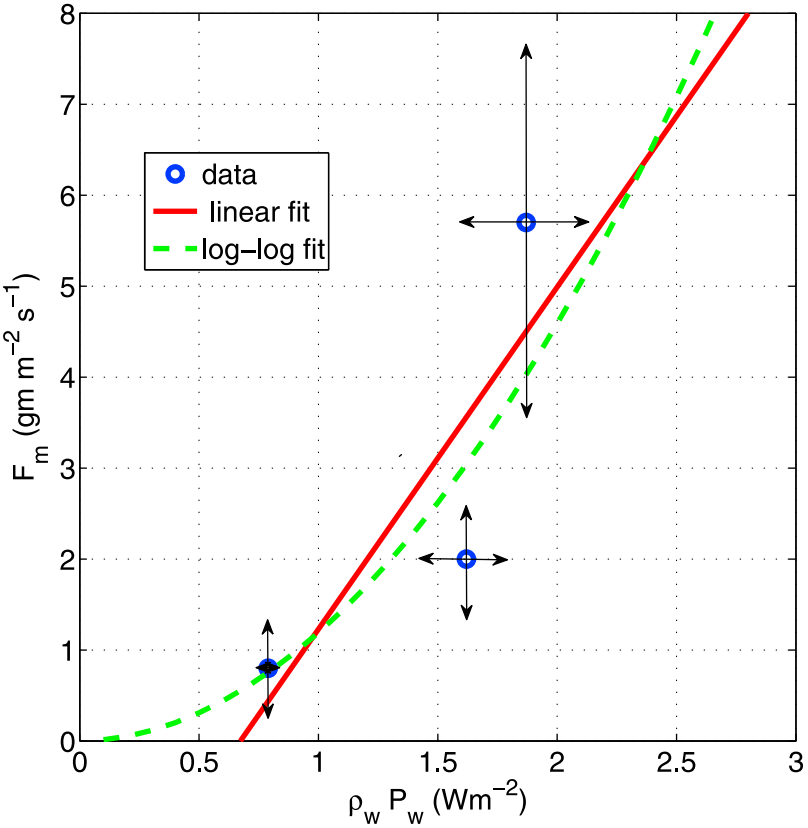

Figure 11. Observed dependence for the 25 ppt salinity case of spray mass flux measured by the CIP probe on the mean breaker surface layer energy flux determined by averaging three different estimates (see section 5.4). Note the significant threshold in the surface disturbance energy flux before a spray flux develops. The horizontal scatter and vertical error bars indicate the uncertainty in these measurements. The solid line is the linear fit, and the dashed line is a log-log (power law) fit.

5.4. Analysis of Breaking Surface Energy Flux

[51] We sought to relate the spray mass flux to an effective wind-forced flux of surface energy fluctuations associated with active breaking crest regions, which requires quantifying the properties of the turbulent region of whitecaps [see *Kudryavtsev*, 2006, Figure 1]. Even in the laboratory it is extremely difficult to directly measure kinetic energy dissipation rate by breaking waves. We made three estimates of this quantity for each wind/wave condition as described in methods 1–3 below, and averaged the results to obtain mean values and the indicative uncertainty.

[52] 1. We used the root mean square surface displacement $\eta_{rms} = \left\langle \sqrt{\eta_{\rm hf}^2} \right\rangle$ of the high frequency wavy oscillations localized around the crests of the breaking dominant wind waves a surface expression of the breaking dissipation rate. This measure reflects the mean potential energy level of the breaker-induced surface fluctuations, phase-averaged along the actively breaking crest region. Extracting the local high frequency surface height fluctuations from the wave elevation signal required subtracting from the total wave height signal an optimally low-pass filtered signal representing the local dominant waveform. In the surface disturbance analysis, η_{rms} is the average over 30 sampling interval partitions, each of approximately 200 s and each corresponding to the passage of O(300) waves. From the resultant residual high frequency "riding" disturbances, the root mean square high frequency surface displacement was calculated, as described in Appendix A.

[53] Our first method for estimating the breaking dissipation rate combines *Terray et al.* [1996] and TKE arguments:

$$\frac{\varepsilon_0 H_s}{P_w} = C_e \tag{25}$$

Here P_w is the kinematic energy flux on the water side (vertical integral of the dissipation rate), H_s is significant wave height, C_e is a constant, and ε_0 is the dissipation rate of TKE at the surface. Standard turbulence theory [*Soloviev and Lukas*, 2006] gives

$$\varepsilon = \frac{q^3}{16 L_b} \tag{26}$$

where $q = (2{*}TKE)^{1/2} = (\sigma_u^2 + \sigma_v^2 + \sigma_w^2)^{1/2}$. Assuming $\sigma_u^2 = \sigma_v^2 = \sigma_w^2 = g\eta_{rms}$, and taking into account the finite extent of the active breaking region, we have $q = (3g\eta_{rms})^{1/2}$, where $\alpha \sim 0.25$ is the fraction of the wavelength supporting the breaker-agitated surface layer fluid. In a turbulent surface shear layer, $L_b = \kappa z$, where κ is the von Karman constant. In the breaking wave layer, *Terray et al.* [1996] give $C_e = 0.83$ and wave turbulent layer depth $L_b \sim 0.6 H_s$ but subsequent papers and measurements [e.g., *Soloviev and Lukas*, 2006]

suggest C_e is closer to 2 and the wave turbulent layer depth $L_b \sim 0.2H_s$, giving

$$P_w = \frac{\alpha}{16 * C_e * L_b/H_s} [3g\eta_{rms}]^{3/2} \quad (27)$$

It should be noted that in this expression for P_w the product $C_e{*}L_b/H_s$ is not sensitive to the choice of value pairs from *Terray et al.* [1996] or *Soloviev and Lukas* [2006].

[54] 2. The atmospheric energy flux to the water surface can be estimated as $\rho_a P_a = \rho_a \bar{c} u_{*a}^2$, where $\bar{c}$, the effective wave phase speed associated with pressure-wave stress, can be estimated using Figure 8 in the work by *Terray et al.* [1996]. Assuming the excess wind input to these very strongly forced young waves is balanced predominantly by wave breaking yields $\rho_a P_a = \rho_a \bar{c} u_*^2 = 0.4 \rho_a u_*^3$.

[55] 3. A third method was used to estimate the breaking dissipation rates using a high resolution wind wave model [*Banner and Morison*, 2006]. Model runs of duration limited wave growth were initiated for extremely young JONSWAP spectra, with initial H_s of several centimeters. A range of 10m-height driving winds, U_{10}, was used from 18 to 36 ms^{-1}. The wind friction velocity and integrated dissipation rate together with the dominant wave properties were produced as the waves evolved. The results were extrapolated over a modest range to younger seas to match the wind friction and wave height conditions in the wave tank experiments. The resulting dissipation rate levels were found to closely match the levels estimated by the other two methods.

[56] The observed relationship between spray mass flux and breaking wave dissipation rate is shown in Figure 11, with horizontal and vertical uncertainty bounds indicated. Two least squares fits (one linear and one log-log) to the data were made and the best fit curves are shown in this figure. The log-log fit gives an exponent very close to quadratic. The chi-square (RMS difference between points and line) are 1.42 and 1.38 $g^{-2}\,s^{-1}$ for the linear and log-log fits, respectively; hence, there is no clear preference for either of these fits. A future investigation using a wider dynamic range of wind and wave conditions is needed to resolve this issue.

[57] It is noteworthy that the dynamic range observed for the spray flux of nearly an order of magnitude was surprisingly large. For comparison, the observed dependence of spray mass flux against the friction velocity u_* is shown in Figure 8. Another interesting feature of the data was evident. As the wind speed was increased, the observed mean wave height was seen to decrease. This is clearly evident for the two highest wind speeds, but is also apparent for the lowest wind speed when the influence of the higher dominant wave frequency for that case is taken into account. This leads to the possibility that the spray flux is enhanced at the expense of the water mass in the dominant wave form, in addition to emanating from the high frequency breaking zone disturbances. However, we did not see any evidence of "flattened" crests where the crest fluid had been 'ripped' from the underlying waveform. The observed large increase in spray flux needs further investigation.

[58] Assuming a linear fit is applicable, the data show a threshold behavior, and the result in Figure 11 can be interpreted as providing the following relationship between the near-surface spray flux F_m and the associated equivalent surface energy flux, P_w, for these specific experimental conditions

$$F_m = MAX[0, s_0 \rho_w (P_w - P_{w\_th})] \quad (28)$$

where $\rho_w P_{w\_th} = 0.7\ Wm^{-2}$ and $s_0 = 3.7 \times 10^{-3}\ s^2 m^{-2}$. This threshold for spume production is significantly greater than the value of (0.013 to 0.038 Wm^{-2}) for whitecap fraction found by *Hwang and Sletten* [2008]. This is consistent with observations that the wind speed threshold for whitecapping is lower than for spume droplet production. For open ocean conditions, 0.7 Wm^{-2} corresponds to a 10-m wind speed of about 10 ms^{-1}. Generalizing this result to other breaker/wind-forcing scales is explored in the following section.

5.5. Scaling/Extrapolation Perspective

[59] The present correlation between spray mass flux, the energy flux to waves, and/or breaker surface disturbance energy flux (Figure 11) was observed for a narrow range of wave scales and forcing wind speeds. To be able to use this correlation more generally, a reliable extrapolation to other wave scales and forcing wind conditions is needed. For example, for our strong forcing case the friction velocity is 1.78 ms^{-1} and the wave breaking energy flux is about 2 Wm^{-2}. In the open ocean, the same value of friction velocity would correspond to a wave breaking energy flux of about 30 Wm^{-2}. If u_* is the fundamental variable to scale droplet mass flux, then the mass flux over the open ocean at $u_* = 1.78$ ms^{-1} would be the same as observed in the wind tunnel at strong forcing. Whereas, if wave breaking energy is the fundamental scaling variable, then we expect about 15 times more droplet mass flux over the ocean at $u_* = 1.78$ ms^{-1} for the linear fit in Figure 11. Incidentally, the log-log fit would imply a mass flux of more than four orders of magnitude larger for wave breaking energy flux of 30 Wm^{-2}. In other words, we can reject the log-log fit as a useful tool for extrapolation. A second factor to consider is the probability droplets at the interface are actually injected into the turbulent flow. This error function factor in equation (B9) is an example of a method to estimate this probability. Conditions in the wind tunnel are ideal for the maximum injection; that is, very strong winds over small, steep waves. Over the open ocean, this factor would be less favorable for large droplets and lower mass flux would result.

[60] Another issue to consider is how to integrate different contributions from a bandwidth of breaking scales. The wind tunnel is essentially monochromatic while the open ocean has a spectrum of waves. To lowest order, a linear breaker dimension such as the along-wind extent scales with the breaker wavelength; the RMS wave height of the high frequency disturbances is assumed to do likewise. The data for the two wavelengths observed in our study conformed to this scaling. According to the proposed surface disturbance energy flux described in the previous section, for a given upstream fetch and for comparable driving wind speeds, the cumulative contribution of a large number of short breakers could be comparable with the net contribution from a much smaller number of larger breakers. For a broad bandwidth of breaking wave scales, the various scale contributions to the surface energy flux would require weighting by their breaking probabilities. Future observations over a wider

range of wave scales are needed to investigate this important scaling issue.

6. Conclusions

[61] SPANDEX used laboratory data to examine scaling relationships for the production of spume sea spray droplets. In section 3, a variety of available scaling approaches from the literature was presented, showing there is no clear consensus on the fundamental parameters of this process, although surface stress, wave breaking energy, and other wave parameters are obvious candidates. Unraveling the fundamental forcing from field measurements is difficult because the various candidates are highly correlated (e.g., whitecap fraction, wave breaking energy, and mean breaking length may all scale as wind speed or friction velocity to a power of 3 to 4). Furthermore, wave breaking energy might scale as $c_p * u_*^2$ but, since c_p is often roughly proportional to u_*, $c_p * u_*^2$ may be experimentally indistinguishable from u_*^3. A laboratory study offers the advantage of controlling some of the parameters independently, for example, one might fix u_* and vary c_p to see the effect on spray production. The disadvantage of a laboratory study is, of course, the need to provide a defensible link between the results and the real world. In our case, we do not claim that the spray source function we measure in the laboratory is the same as over the ocean. Rather, we assert that the wind stress interactions with breaking waves in the laboratory are reasonably similar to oceanic waves. Thus, we can explore fundamental scaling behavior of the spray production.

[62] Our observations of droplet profiles (Figure 5 versus Figure 6) give reasonable confirmation of the basic profile relationship (11) that is commonly used to relate droplet concentrations to the surface source strength. This also confirms that even in a wind tunnel, the constant flux profile (4) is approximately valid. The PDA observations revealed significant mean horizontal and vertical slip velocities that were larger closer to the surface (Figures 8 and 9). The magnitude seems too large to be an acceleration time scale effect, so we hypothesize that the droplets tend to be found in vertically moving air masses (e.g., updrafts departing from wave crests). Scaling of the droplet production surface source strength proved to be difficult to explain. The wind speed forcing varying only 23% and the stress increased a factor of 2.2. Yet, the source strength increased by about a factor of 7 (Figures 8 and 11). We attempted to relate this to an estimate of surface wave energy flux through calculations of the standard deviation of small-scale surface disturbance; this index was found to be quite close to an independent estimate of the wind input to the waves and a numerical wave model calculation of wave dissipation for the wind tunnel conditions. This energy index only increased by a factor of 2.3 with the wind forcing, so it is not clear that we have characterized P_b correctly. Nonetheless, a graph of spray mass surface flux versus surface disturbance energy is quasi-linear with a substantial threshold.

Appendix A

[63] Since the local dominant waveform is modulated in both frequency and amplitude, we introduced a phase-averaged approach. The zero crossings of the dominant wave signal $z = \eta$ formed the basis for setting up a 50 point phase space for the $\eta > 0$ region of the dominant wave. Each phase bin accumulated the respective deviation of the actual wave height from the local dominant wave elevation. Phase averaging of the squared deviation provided the local distribution of breaking-induced disturbance potential energy. We noted that at the highest wind speed, a significant reduction was observed in the dominant wave height associated with the increased strength of the breaking events.

[64] The wave height signal was composed of a relatively steep dominant wave with superimposed high-frequency disturbances, including spikes from water droplets impacting the wave wires. The data were despiked subsequently with a detection and replacement code. To extract the dominant wave signal from the total wave height signal, several low-pass filtration techniques were investigated. The steepness of the dominant waveform provided a very considerable challenge. As with most filtering techniques, some arbitrariness is implicit in the choice of "optimal" filter parameters and we used visual inspection of the low-passed signal superposed on the original signal to choose the most appropriate technique. We finally chose a smooth spline method using the Matlab routine *spaps.m*. With this technique the fitted spline does not pass through each data point, but represents a least squares fit to the data trend for a given spline tension. Adjusting the tension allows fitting the low-frequency dominant wave while smoothing over the high-frequency roughness elements associates with the breaking. Optimizing the spline tension is crucial in this analysis, and is described in detail below.

[65] For an initial choice of spline tension, the smooth spline was applied to the whole elevation data record. The typical ensemble size was about 400,000 points, or 6000 waves. The mean difference $\langle\Delta\rangle$ between the actual surface elevation and the smoothed surface elevation was calculated over the data record, and the degree of filtering assessed visually for removal of the high-frequency features and goodness of fit to the dominant wave form. Because of differences in the dominant wave frequencies and wave heights, a given spline tension value had different filtering effects on the wave height signal for these various cases. We chose a different tension value for each case to conform to the common upper bound of 2 mm for the mean difference $\langle\Delta\rangle$, and to have the same visual degree of filtering. The high-frequency data were then despiked with a detection code based on local signal gradient and the spike region was replaced locally with a cubic interpolation.

[66] Typical results are visualized below in Figure A1, which shows a small segment of the data and the low-pass filtered signal which yields the local surface fluctuation signal. Following the choice of appropriate spline tension, the zero crossings of the smoothed wave profile were identified. Each crest subdomain ($\eta > 0$) was divided into 50 phase segments. The distribution of the phase averaged high-frequency disturbance energy was found similarly from the square of the deviation between the actual surface and the smoothed surface at each phase point, which was then phase averaged over the ensemble.

[67] Typical results for the phase averaged kinematic wave energy and breaking disturbance energy distributions are shown in Figure A2. Visual inspection shows that these choices were reasonable. The equivalent high-frequency

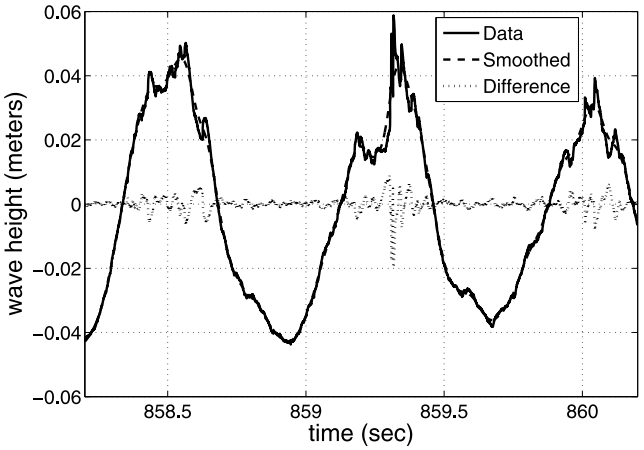

Figure A1. Typical wave height data for 17.8 ms^{-1} wind speed sampled at 2322 Hz, with the superimposed dominant wave obtained by smooth spline filtration. The high-frequency breaking disturbance height signal is the difference between these, shown as the small high-frequency signal oscillating about the zero wave height axis.

disturbance height distribution was then used to construct the mean dissipation rate due to wave breaking described in section 5.4. For this calculation, only a subset of the 50 point distribution was used, namely the phase points spanning the "active crest region." This spanned 25 points centered on the phase-averaged wave crest maximum for each case. This allowed us to include the physically relevant breaker disturbance contributions, while minimizing any residual errors in fitting the very steep forward faces of some of the dominant waves.

Appendix B

[68] The physically based sea spray model of Fairall and Banner (manuscript in preparation, 2009) is based on the assumption that some fraction of the energy going into wave breaking is consumed by breakdown of the interface into droplets and bubbles. The actual droplet source function is then the number produced at the interface times the probability that wind gusts near the interface are able to accelerate the droplets into the turbulent surface layer. Following *Andreas* [1998], we represent the rate of turbulent kinetic energy (TKE) converted to potential energy in the surface tension of droplets as

$$\frac{\partial \Delta\Omega}{\partial t} = \Gamma \int_0^\infty \frac{4}{3}\pi r^2 n_s(r) dr \tag{B1}$$

where $\Delta\Omega$ is some small fraction of the total energy input, $\rho_w P$, to breaking waves (Wm^{-2}), Γ the surface tension of the water-air interface (Nm^{-1}), r the droplet radius, and $n_s(r)$ the number of droplets produced per second per square meter of surface. We assume that the energy to produce the droplets comes from the turbulent cascade of TKE from the breaking scale to the dissipation scale. From *Tennekes and Lumley* [1972], the energy spectral density in wave number space, $E(k)$, is

$$E(k) = \alpha_K \varepsilon^{2/3} k^{-5/3} \exp\left[-\frac{3}{2}\alpha_k (k\eta_k)^{4/3}\right] \tag{B2}$$

where ε is the rate of dissipation of TKE

$$\varepsilon = 2\nu \int_0^\infty k^2 E(k) dk \tag{B3}$$

Here $\eta_k = (\nu^3/\varepsilon)^{1/4}$ is the Kolmogorov microscale, α_k is the Kolmogorov constant ($\approx$0.54), and ν is the kinematic viscosity of the fluid. In dynamic equilibrium, $E(k)$ is related to the rate of spectral energy transfer in wave number space, $T(k)$, by

$$\frac{\partial T(k)}{\partial k} = -2\nu k^2 E(k) \tag{B4}$$

Since we are interested in droplets of some size, we transform from a wave number spectrum to a size spectrum, $T(r)$. We assume that $k = \pi/r$ and TKE is conserved in density space [$E(k)dk = E(r)dr$]. It then follows that in the inertial subrange, $T(r)$ is given by

$$T(r) = \varepsilon \exp\left[-\frac{9}{4}\alpha_k \left(\frac{\pi\eta}{r}\right)^{4/3}\right] \tag{B5}$$

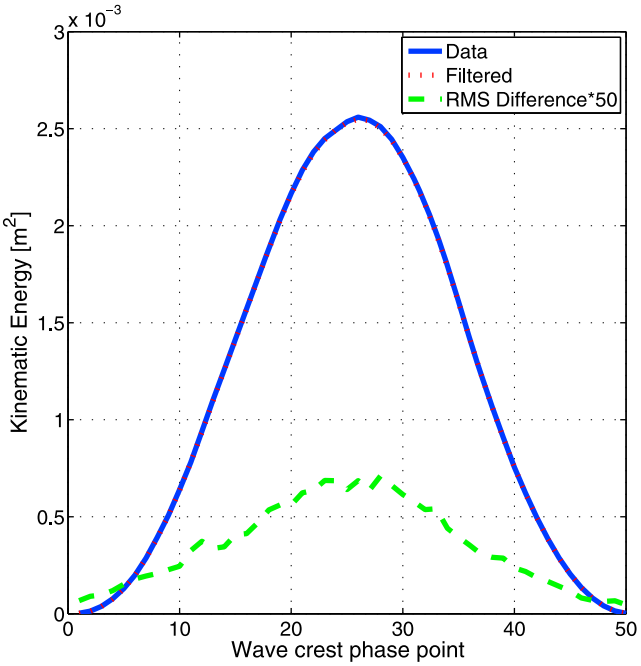

Figure A2. The phase-averaged wave kinematic energy (surface height squared) and mean square breaker disturbance energy for 17.8 ms^{-1} wind speed plotted against the wave crest phase point, where the 50 points span the wave crest region. Note the unfiltered ("Data") and filtered ("Filtered") phase-averaged mean squared wave height signals are indistinguishable. The breaker disturbance mean-squared height has been multiplied by a factor of 50.

Now, we relate energy input per unit area, P, versus energy dissipated near the surface (per unit volume). The total wave dissipation is distributed vertically such that

$$P = \int \varepsilon(z)dz \approx \varepsilon_0 L_b \tag{B6}$$

where L_b is a characteristic depth scale for breaking wave turbulence near the surface of a breaking wave and ε_0 the dissipation rate near the interface on the ocean side.

[69] We now assume that some *small* fraction, f_d, of the energy being transferred in r space is lost to the droplets. This implies

$$\frac{4}{3}\Gamma\pi r^2 n_s(r) = f_d \rho_w T(r) \tag{B7}$$

where T is the value in the region very close to the interface. This gives a final expression for n_s expressed as the droplet volume flux

$$\frac{4\pi r^3}{3} n_s(r) = \frac{f_d \,\mathrm{Pr}}{\sigma L_b} \exp\left[-\frac{9}{4}\alpha_k \left(\frac{\pi\eta}{r}\right)^{4/3}\right] \tag{B8}$$

where $\sigma = \Gamma/\rho_w = 7.4 * 10^{-5}$ m^3 s^{-2} and we have assumed that the "appropriate" size scale describing the dissipation rate near the surface on the upwind side of the breaking wave is proportional to L_b (so that f_d now incorporates an additional factor).

[70] This approach gives an estimate of the droplet spectrum produced by the breakdown of the air-water interface, but it says little about the introduction of those droplets into the turbulent surface layer over the water. To do this, we postulate that the large droplets will be accelerated along the windward face of the breaker, blown off the top of the wave and execute a nearly ballistic trajectory into the trough ahead of the breaker. They will spend a significant time airborne if their fall velocity is less than the local wind speed near the wave crest times the local slope of the waves. If we assume a Gaussian distribution of horizontal wind speed fluctuations, then an error function describes the integral probability that a droplet of size r is ejected from the top of the wave. Thus

$$\frac{4\pi r^3}{3} n_s(r) = \frac{f_d \,\mathrm{Pr}}{\sigma L_b} \exp\left[-\frac{9}{4}\alpha_k \left(\frac{\pi\eta}{r}\right)^{4/3}\right] * \left[1 + erf\left(\frac{U_d(h) + U_b - V_g/Slope}{\sigma_u}\right)\right] \Big/ 2 \tag{B9}$$

where $V_g(r)$ is the gravitational settling speed of the droplet, $U_d(h)$ the mean wind speed at height h, U_b the forward speed of the breaking wave top, and σ_u the standard deviation of wind speed fluctuations at h. For large droplets, low wind speeds, or small wave slopes the argument of the error function would be significantly negative [erf($-\infty$) = -1] and no droplets are observed. For very small droplets, η_k/r becomes large, and no droplets are produced because it takes too much energy to overcome surface tension. For the simulation discussed in Figure 8, we specified L_b = 0.1 m, f_d = 0.02, *Slope* = 0.09, and $\sigma_u = 0.6 \times U_{10}$. A more detailed derivation and *Matlab* codes for this model can be found at ftp://ftp.etl.noaa.gov/user/cfairall/onr_droplet/parameterization/.

Notation

$a(r)$	size-dependent sample area of CIP.
c_p	wave phase speed.
$\bar{c}$	mean wave phase speed associated with pressure input to the wave growth.
dr	droplet radius increment, as in CIP size resolution.
dt	particle sample time interval.
f_d	fraction of TKE spectral transfer that is consumed to form droplets.
$f_n(r)$	whitecap-normalized particle source size distribution.
f_p	wave maker paddle frequency.
f_s	factor characterizing reduction of turbulent diffusion for large particles.
h	wave height (one-half the significant wave height).
k	turbulent fluctuation wave number.
$n(r)$	droplet concentration size spectral density.
n'	fluctuation in droplet concentration.
$n_s(r)$	droplet source size spectral density right at the air-water interface.
r	particle radius.
r_m	maximum particle radius permitted by viscous forces.
s_o	linear slope of particle mass flux and surface disturbance energy.
t	time.
u'	horizontal velocity fluctuation.
w'	vertical velocity fluctuation.
w_s'	particle vertical slip velocity fluctuation.
$\overline{w'n'}$	vertical turbulent flux of particles.
$\overline{w_s'n'}$	vertical turbulent flux of particles associated with slip-particle correlations.
$\overline{w'u'}$	vertical turbulent flux of particles.
z	height above mean surface level.
z_o	surface roughness length.
Ce	ratio of H_s* ε_o to P_w.
D_p	molecular diffusion coefficient for particles.
$E(k)$	spectral energy density for turbulent fluctuations.
F_A	droplet area flux from *Kudryavtsev* [2006].
F_z	total vertical flux of particles.
F_m	mass flux of particles estimated at the interface.
F_o	total vertical flux of particles at the interface.
H_s	significant wave height.
$K(z)$	turbulent eddy diffusion coefficient.
$K_p(z)$	turbulent eddy diffusion coefficient for particles.
L_b	vertical length scale of breaking wave dissipation region.
$M(z)$	suspended particle mass as a function of height.
P	energy flux (kinematic) from atmosphere to the ocean.
P_b	energy flux to wave breaking.
P_{w_th}	energy flux threshold (water side) for breaking.
Q_n	volume source function for particles.
R_u	stress capillary wave scaling parameter.
S_n	area source function for particles.
$T(k)$	rate of spectral energy transfer for turbulent fluctuations.

U wind speed.
U_d mean wind speed at h.
U_t wind speed near wave tops.
U_{ref} wind speed from reference at tunnel entrance from hot film sensor.
U_x horizontal droplet velocity.
U_z vertical droplet velocity.
$V(r)$ volume of droplet of radius r.
V_g particle mean gravitational fall velocity.
W whitecap areal fraction.
W_A wave age
α fraction of the surface-supporting breaker agitated surface layer fluid.
α_k Kolmogorov constant (0.54).
ε rate of dissipation of turbulent kinetic energy.
ε_o rate of dissipation of turbulent kinetic energy near the interface on the oceanside.
η water surface elevation.
η_{hf} high-pass filtered surface elevation.
η_k Kolmogorov microscale.
κ Von Karman constant (0.4).
λ surface gravity wavelength.
ρ_a density of air.
ρ_w density of water.
σ kinematic surface tension of water-air interface (Γ/ρ_w).
σ_u horizontal velocity standard deviation.
σ_w vertical velocity standard deviation.
τ horizontal momentum flux ($\overline{w'u'}/\rho_a$).
ν kinematic viscosity of air.
$\langle\Delta\rangle$ mean surface displacement from smooth wave function.
Γ surface tension of water-air interface.
Λ mean wave-breaking length per unit area.

[71] **Acknowledgments.** The authors wish to thank the staff of the Water Research Laboratory, School of Civil and Environmental Engineering of the University of New South Wales, for their outstanding efforts that made this study possible. This work was supported by the Office of Naval Research under the CBLAST Departmental Research Initiative and the NOAA Hurricane Intensity Research Project.

References

Andreas, E. L. (1992), Sea spray and the turbulent air-sea heat fluxes, *J. Geophys. Res.*, *97*, 11,429–11,441, doi:10.1029/92JC00876.

Andreas, E. L. (1998), A new spray generation function for wind speeds up to 32 ms^{-1}, *J. Phys. Oceanogr.*, *28*, 2175–2184, doi:10.1175/1520-0485(1998)028<2175:ANSSGF>2.0.CO;2.

Andreas, E. L. (2002), A review of the sea spray generation function for the open ocean, in *Atmosphere-Ocean Interactions*, vol. 1, edited by W. Perrie, pp. 1–46, WIT Press, Southampton, U. K.

Andreas, E. L. (2004), Spray stress revisited, *J. Phys. Oceanogr.*, *34*, 1429–1440, doi:10.1175/1520-0485(2004)034<1429:SSR>2.0.CO;2.

Andreas, E. L., and K. A. Emanuel (2001), Effects of sea spray on tropical cyclone intensity, *J. Atmos. Sci.*, *58*, 3741–3751, doi:10.1175/1520-0469(2001)058<3741:EOSSOT>2.0.CO;2.

Andreas, E. L., J. B. Edson, E. C. Monahan, M. P. Rouault, and S. D. Smith (1995), The spray contribution to net evaporation from the sea–A review of recent progress, *Boundary Layer Meteorol.*, *72*, 3–52, doi:10.1007/BF00712389.

Anguelova, M., R. P. Barber, and J. Wu (1999), Spume drops produced by the wind tearing of wave crests, *J. Phys. Oceanogr.*, *29*, 1156–1165, doi:10.1175/1520-0485(1999)029<1156:SDPBTW>2.0.CO;2.

Banner, M. L., and R. P. Morison (2006), Modeling spectral dissipation due to wave breaking for ocean wind waves, paper presented at 9th International Workshop On Wave Hindcasting and Forecasting, Environ. Canada, Victoria, B. C., Canada, 24–29 Sept.

Bao, J.-W., J. M. Wilczak, J.-K. Choi, and L. Kantha (2000), Numerical simulations of air-sea interaction under high wind conditions using a coupled model: A study of hurricane development, *Mon. Weather Rev.*, *128*, 2190–2210, doi:10.1175/1520-0493(2000)128<2190:NSOASI>2.0.CO;2.

Barenblatt, G. I., A. J. Chorin, and V. M. Prostokishin (2005), A note concerning the Lighthill "sandwich model" of tropical cyclones, *Proc. Natl. Acad. Sci. U. S. A.*, *102*, 11,148–11,150, doi:10.1073/pnas.0505209102.

Bauckhage, K. (1988), The Phase-Doppler-difference-method, a new Laser-Doppler technique for simultaneous size and velocity measurements. Part 1. Description of method, *Part. Part. Syst. Charact.*, *5*, 16–22, doi:10.1002/ppsc.19880050105.

Baumgardner, D., and A. Korolev (1997), Airspeed corrections for optical array probe sample volumes, *J. Atmos. Oceanic Technol.*, *14*, 1224–1229, doi:10.1175/1520-0426(1997)014<1224:ACFOAP>2.0.CO;2.

Black, P. G., et al. (2007), Air-sea exchange in hurricanes—Synthesis of observations from the coupled boundary layer air-sea transfer experiment, *Bull. Am. Meteorol. Soc.*, *88*, 357–375.

Bye, J. A. T., and A. D. Jenkins (2006), Drag coefficient reduction at very high wind speeds, *J. Geophys. Res.*, *111*, C03024, doi:10.1029/2005JC003114.

Drennan, W. M., J. A. Zhang, J. R. French, C. McMormick, and P. G. Black (2007), Turbulent fluxes in the hurricane boundary layer. Part II: Latent heat flux, *J. Atmos. Sci.*, *64*, 1103–1115, doi:10.1175/JAS3889.1.

Edson, J. B., and C. W. Fairall (1994), Spray droplet modeling: Part 1. Lagrangian model simulation of the turbulent transport of evaporating droplets, *J. Geophys. Res.*, *99*, 25,295–25,311, doi:10.1029/94JC01883.

Edson, J. B., and C. W. Fairall (1998), Similarity relationships in the marine atmospheric surface layer for terms in the TKE and scalar variance budgets, *J. Atmos. Sci.*, *55*, 2311–2338, doi:10.1175/1520-0469(1998)055<2311:SRITMA>2.0.CO;2.

Emanuel, K. A. (1995), Sensitivity of tropical cyclones to surface exchange coefficients and a revised steady-state model incorporating eye dynamics, *J. Atmos. Sci.*, *52*, 3969–3976, doi:10.1175/1520-0469(1995)052<3969:SOTCTS>2.0.CO;2.

Emanuel, K. A. (1999), Thermodynamic control of hurricane intensity, *Nature*, *401*, 665–669, doi:10.1038/44326.

Emanuel, K. A. (2003), A similarity hypothesis for air-sea exchange at extreme wind speeds, *J. Atmos. Sci.*, *60*, 1420–1428, doi:10.1175/1520-0469(2003)060<1420:ASHFAE>2.0.CO;2.

Fairall, C. W., and S. E. Larsen (1984), Dry deposition, surface production, and dynamics of aerosols in the marine boundary layer, *Atmos. Environ.*, *18*, 69–77, doi:10.1016/0004-6981(84)90229-4.

Fairall, C. W., K. L. Davidson, and G. E. Schacher (1983), An analysis of the surface production of sea-salt aerosols, *Tellus Ser. B*, *35*, 31–39.

Fairall, C. W., J. B. Edson, and M. A. Miller (1990), Heat fluxes, whitecaps, and sea spray, in *Surface Waves and Fluxes: Current Theory and Remote Sensing*, edited by G. L. Geernaert and W. J. Plant, pp. 173–208, Kluwer Academic, Dordrecht, Netherlands.

Fairall, C. W., J. D. Kepert, and G. H. Holland (1994), The effect of sea spray on surface energy transports over the ocean, *Global Atmos. Ocean Syst.*, *2*, 121–142.

Fairall, C. W., E. F. Bradley, J. E. Hare, A. A. Grachev, and J. B. Edson (2003), Bulk parameterization of air-sea fluxes: Updates and verification for the COARE algorithm, *J. Clim.*, *16*, 571–591, doi:10.1175/1520-0442(2003)016<0571:BPOASF>2.0.CO;2.

French, J. R., W. M. Drennan, J. A. Zhang, and P. G. Black (2007), Turbulent fluxes in the hurricane boundary layer. Part I: Momentum flux, *J. Atmos. Sci.*, *64*, 1089–1102, doi:10.1175/JAS3887.1.

Garrett, C., M. Li, and D. Farmer (2000), The connection between bubble size spectra and energy dissipation rates in the upper ocean, *J. Phys. Oceanogr.*, *30*, 2163–2171, doi:10.1175/1520-0485(2000)030<2163:TCBBSS>2.0.CO;2.

Hinze, J. O. (1955), Fundamentals of the hydrodynamic mechanism of splitting in dispersion processes, *AIChE J.*, *1*, 289–295.

Hoppel, W. A., G. M. Frick, and J. W. Fitzgerald (2002), Surface source function for sea-salt aerosol and aerosol dry deposition to the ocean surface, *J. Geophys. Res.*, *107*(D19), 4382, doi:10.1029/2001JD002014.

Hwang, P. A., and M. A. Sletten (2008), Energy dissipation of wind-generated waves and whitecap coverages, *J. Geophys. Res.*, *113*, C02012, doi:10.1029/2007JC004277.

Kepert, J. D., C. W. Fairall, and J.-W. Bao (1999), Modeling the interaction between the atmospheric boundary layer and evaporating sea spray droplets, in *Air-Sea Fluxes: Momentum, Heat, and Mass Exchange*, edited by G. L. Geernaert, pp. 363–409, Kluwer Academic, Dordrecht, Netherlands.

Knollenberg, R. G. (1970), The optical array: An alternative to scattering or extinction for airborne particle size determination, *J. Appl. Meteorol.*, *9*, 86–103, doi:10.1175/1520-0450(1970)009<0086:TOAAAT>2.0.CO;2.

Koga, M. (1986), Characteristic features of a wind wave field with occasional breaking, and splashing droplets at high winds, in *Oceanic White-*

caps, edited by E. C. Monahan and G. Mac Niocaill, pp. 129–145, D. Reidel, Dordrecht, Netherlands.

Kudryavtsev, V. N. (2006), On the effect of sea drops on the atmospheric boundary layer, *J. Geophys. Res.*, *111*, C07020, doi:10.1029/2005JC002970.

Lewis, E. R., and S. E. Schwartz (2004), *Sea Salt Aerosol Production: Mechanisms, Methods, Measurements, and Models—A Critical Review*, *Geophys. Monogr.*, vol. 152, AGU, Washington, D. C.

Li, W. (2004), Modeling air-sea fluxes during a western Pacific typhoon: Role of sea spray, *Adv. Atmos. Sci.*, *21*, 1867–1883.

Makin, V. K. (1998), Air-sea exchange of heat in the presence of wind waves and spray, *J. Geophys. Res.*, *103*, 1137–1152, doi:10.1029/97JC02908.

Makin, V. K. (2005), A note on the drag of the sea surface at hurricane winds, *Boundary Layer Meteorol.*, *115*, 169–176, doi:10.1007/s10546-004-3647-x.

Monahan, E. C. (1989), From the laboratory tank to the global ocean, in *The Climate and Health Implications of Bubble-Mediated Sea-Air Exchange*, edited by E. C. Monahan and M. A. Van Patten, pp. 43–63, Conn. Sea Grant Coll. Program, Groton, Conn.

Monahan, E. C., and I. G. O' Muircheartaigh (1980), Optimal power-law description of oceanic whitecap coverage dependence on wind, *J. Phys. Oceanogr.*, *10*, 2094–2099, doi:10.1175/1520-0485(1980)010<2094:OPLDOO>2.0.CO;2.

Newell, A. C., and V. E. Zakharov (1992), Rough sea foam, *Phys. Rev. Lett.*, *69*, 1149–1151, doi:10.1103/PhysRevLett.69.1149.

Powell, M. D., P. J. Vickery, and T. A. Reinhold (2003), Reduced drag coefficient for high wind speeds in tropical cyclones, *Nature*, *422*, 279–283, doi:10.1038/nature01481.

Smith, M. H., and N. M. Harrison (1998), The sea spray generation function, *J. Aerosol Sci.*, *29*, suppl. 1, S189–S190, doi:10.1016/S0021-8502(98)00280-8.

Smith, M. H., P. M. Park, and I. E. Consterdine (1993), Marine aerosol concentrations and estimated fluxes over the sea, *Q. J. R. Meteorol. Soc.*, *119*, 809–824, doi:10.1002/qj.49711951211.

Soloviev, A., and R. Lukas (2006), *The Near-Surface Layer of the Ocean*, 572 pp., Springer, Dordrecht, Netherlands.

Tennekes, H., and J. L. Lumley (1972), *A First Course in Turbulence*, 300 pp., MIT Press, Cambridge, Mass.

Terray, E. A., M. A. Donelan, Y. C. Agrawal, W. M. Drennan, K. K. Kahma, A. J. Williams, P. A. Hwang, and S. A. Kitaigorodskii (1996), Estimates of kinetic energy dissipation under breaking waves, *J. Phys. Oceanogr.*, *26*, 792–807, doi:10.1175/1520-0485(1996)026<0792:EOKEDU>2.0.CO;2.

Toba, Y. (1970), On the giant sea-salt particles in the atmosphere: Part I. General features of the distribution, *Tellus*, *17*, 131–145.

Wang, Y., J. D. Kepert, and G. J. Holland (2001), The effect of sea spray evaporation on tropical cyclone boundary layer structure and intensity, *Mon. Weather Rev.*, *129*, 2481–2500, doi:10.1175/1520-0493(2001)129<2481:TEOSSE>2.0.CO;2.

Zhao, D., Y. Toba, K. Sugioka, and S. Komon (2006), New sea spray generation function for spume droplets, *J. Geophys. Res.*, *111*, C02007, doi:10.1029/2005JC002960.

W. Asher, Applied Physics Laboratory, University of Washingon, 1013 NE 40th Street, Seattle, WA 98105 -6698, USA.

M. L. Banner, R. P. Morison, and W. L. Peirson, School of Mathematics and Statistics, University of New South Wales, Sydney, NSW 2052, Australia.

C. W. Fairall, Earth System Research Laboratory, NOAA, R/PSD03, Boulder, CO 80305-3337, USA. (chris.fairall@noaa.gov)